Astronomy & Astrophysics manuscript no. Nano-JASMINE
March 1, 2013

© ESO 2013

arXiv:1302.7097v1 [astro-ph.GA] 28 Feb 2013

Astrometric mock observations for determining the local dark matter density

Shigeki Inoue[1,2⋆] and Naoteru Gouda[1]

[1] National Astronomical Observatory of Japan, Mitaka, Tokyo 181-8588, Japan
[2] Korea Astronomy and Space Science Institute 776, Daedeokdae-ro, Yuseong-gu, Daejeon, 305-348, Republic of Korea

Received February 15, 2013; accepted ???? ??, ????

ABSTRACT

Context. To determine the local dark matter density around the solar system is a classical problem in astronomy. Recently, Garbari et al. have devised a novel method to determine the local dark matter density from stellar distribution and vertical velocity dispersion profiles perpendicular to the Galactic plane. Their method has the advantages of abolishing conventional approximations and using only a few assumptions. Their determinations, however, preferred relatively high dark matter densities, which are inconsistent with other recent works.

Aims. The first aim of this paper is to carefully scrutinize the Garbari et al. method. It should be investigated whether the discrepancy between Garbari et al. and the others can be attributed to systematic biases inherent in their method. The second aim is to examine influences by observational uncertainties. We discuss how the determinations of the local dark matter density vary with observational precisions on parallax, proper motion and line-of-sight velocity measurements.

Methods. To examine the influences by the observational imprecision, we create mock observation data for stars being dynamical tracers based on an analytical galaxy model and apply parametrized observational errors to the mock data. We evaluate the accuracy of determining the dark matter density by applying the Garbari et al. method to the mock data. In addition, we estimate a sample size and observational precision to determine the dark matter density with accuracy.

Results. We find that the Garbari et al. method is capable of determining the local dark matter density with accuracy if the sample size and observational precisions are satisfactory. The required sample size is approximately 6,000 stars. However, the parallax and proper motion errors can cause overestimation of the dark matter density. We estimate the required precisions of the parallax measurements to be approximately 0.1–0.3 milliarcseconds; the proper motion precisions do not seem to be as important as the parallax errors. Also, we find that the line-of-sight velocity errors can cause either underestimation or overestimation of the dark matter density, which is contingent on distance-dependence of the errors.

Conclusions. From these results, we infer that Garbari et al. would be overestimating the local dark matter density due to use of imprecise data from the *Hipparcos* catalog; however, we emphasize the capability of their method. We expect that *Gaia* will provide data precise enough to determine the local dark matter density using the Garbari et al. method.

Key words. Methods: analytical – Astrometry – Galaxy: kinematics and dynamics – solar neighborhood – dark matter

1. Introduction

In recent years, dedicated searches for candidates of dark matter (DM) particles have intensified. Experiments aiming at direct detection of the DM particles look for signals from recoil of DM particles with nuclei inside the detector (e.g., Spooner 2007; Baudis 2012, and references therein). Thus, the event rates of the direct detection are clearly proportional to the local DM density (LDMD) around the solar system, $\rho_{\rm dm}^{\odot}$. However, the event rates have degeneracy between the LDMD and cross-sections of the DM particles, therefore we cannot determine the cross-sections without knowledge of the LDMD. This is why the problem of determining the LDMD at the solar position has recently been attracting a great deal of attention.

Because of the "dark" nature, however, it is difficult to understand details of the structures and density distribution of the Galactic DM halo. Usually, we have to resort to dynamical analyses of observable phenomena, such as motions of stars, gas and satellite galaxies. For example, a rotation velocity curve of the Galactic disk is often used to measure the DM halo mass and density profile (e.g., Allen & Martos 1986; Allen & Santillan 1991; Sofue et al. 2009; Irrgang et al. 2013); Sofue (2012)[1] has recently estimated that $\rho_{\rm dm}^{\odot} = 0.00612 \pm 0.00080$ M$_\odot$ pc^{-3}; the other recent works also proposed $\rho_{\rm dm}^{\odot} \lesssim 0.01$ M$_\odot$ pc^{-3}.[2] However, the analyses using rotation curves posit global mass-modelings and a spherical assumption of the Galactic halo. If the Galactic DM halo is far from a round shape, the rotation curve analyses can lead to erroneous determinations since estimated LDMDs are spherically averaged densities (e.g., Zemp et al. 2009). Cosmological simulations have indeed shown that DM halos are generally aspherical (e.g., Dubinski & Carlberg 1991; Allgood et al. 2006; Bett et al. 2007; Kuhlen et al. 2007). Moreover, recent studies on dynamical analyses of the Sagittarius stream have preferred a nearly oblate halo in which the minor axis is approximately aligned with the line of sight to the Galactic center (e.g., Law & Majewski

---

⋆ e-mail: `shigeki.inoue@nao.ac.jp`

[1] Sofue (2012) used an extrapolation of a Navarro-Frenk-White density profile, which is determined by fitting to outer Galactic regions. However, he mentioned that his rotation curve inside $R \sim 20$ kpc cannot constrain the DM density profile.

[2] 1 M$_\odot$ pc^{-3} $\simeq$ 38.0000 GeV cm^{-3}

2010; Ibata et al. 2012; Deg & Widrow 2013,[3] although see Olling & Merrifield 2001; Debattista et al. 2013). Thus, more accurate determination of the LDMD requires following a more direct methodology than modeling the whole halo.

Some studies have tried to determine the LDMD with analyses of local kinematics. For example, Salucci et al. (2010) used an equation of centrifugal equilibrium and an observed local radial gradient of the rotation curve: They determined $\rho_{\rm dm}^{\odot} = 0.0113 \pm 0.0055$ M$_\odot$ pc^{-3}. In addition, other methods of fitting various dynamical parameters, such as Galactic rotations, halo masses and thicknesses of gas layers, also derived LDMDs of $\rho_{\rm dm}^{\odot} \simeq 0.01$ M$_\odot$ pc^{-3} (Olling & Merrifield 2000, 2001; Weber & de Boer 2010; Catena & Ullio 2010). These methods relying on the Galactic rotations and its gradients, however, still posit axisymmetric assumptions.

As another approach, vertical motions of disk stars near the sun are frequently used to determine the LDMD. The Galactic potential of visible and invisible matters (i.e., the total density) can be derived from zenithal profiles of density and velocity dispersion of tracer stars via the Boltzmann and Poisson (or Jeans) equations (e.g., Oort 1932; Bahcall 1984b; Kuijken & Gilmore 1989c). The visible matter density is measured by observations and can be subtracted from the total density, and then one can determine the invisible matter density. This method is advantageous in terms of being independent from the global shape of the DM halo. Previous studies have determined that $\rho_{\rm dm}^{\odot} \lesssim 0.01$ M$_\odot$ pc^{-3} (e.g., Bienayme et al. 1987; Creze et al. 1989; Kuijken & Gilmore 1989a,b; Kuijken 1991; Flynn & Fuchs 1994; Pham 1997; Creze et al. 1998; Holmberg & Flynn 2004; Bovy & Tremaine 2012; Zhang et al. 2012)[4] although some earlier works indicated a preference for much higher LDMDs (e.g., Oort 1932, 1960; Hill 1960; Bahcall 1984a,c).

Recently, Garbari et al. (2011, 2012, hereafter G11 and G12, respectively) have devised a new method to determine the LDMD from stellar motions perpendicular to the Galactic disk. Their method was named the minimal assumption (MA) method and uses, as the name suggests, only a few assumptions and a flexible 15-component galaxy model (see Sect. 2). With the MA method, they determined the LDMDs of $\rho_{\rm dm}^{\odot} = 0.033^{+0.008}_{-0.009}$ M$_\odot$ pc^{-3} in G11 and $\rho_{\rm dm}^{\odot} = 0.022^{+0.013}_{-0.015}$ M$_\odot$ pc^{-3} in G12. Their results are higher than the conventional LDMD by a factor of two or more. They suggested that the discrepancy from the low LDMD derived from Galactic rotations can be indicative of existence of a "dark disk" (Read et al. 2009). However, Zhang et al. (2012) more recently determined $\rho_{\rm dm}^{\odot} = 0.0065 \pm 0.0023$ M$_\odot$ pc^{-3} with a similar but different method, whose sample stars are much larger in number than those of G11 and G12 and carefully selected in an [Fe/H]-[α/Fe] distribution. Since the LDMD determined by Zhang et al. (2012) is comparable to the estimation from rotation curves, they suggested that the Galactic DM halo would be almost spherical and there is no need to consider the existence of a dark disk. In addition, Bovy & Tremaine (2012) also determined $\rho_{\rm dm}^{\odot} = 0.008 \pm 0.003$ M$_\odot$ pc^{-3} from kinematics of thick disk stars.

The MA method of Garbari et al. relying on only a few assumptions seems to be a promising method, although their results are discrepant from the conventional LDMD. They seemed to show that methods of Holmberg & Flynn (2004) and Kuijken & Gilmore (1989a,b,c) have systematic biases to underestimate the LDMD due to unsuitable assumptions of separable distribution function and isothermality for tracer stars. The MA method, on the other hand, does not need these assumptions. Moreover, they applied the MA method to N-body simulation data, and demonstrated that their method can determine the LDMD within the 90 % confidence level. However, as mentioned above, the more recent works by Zhang et al. (2012) and Bovy & Tremaine (2012), which also exclude these disputed assumptions, support the conventional lower LDMD. What is the cause of the inconsistency between Garbari et al. and the others? As our first aim, we examine the capability of the MA method by applying it to mock observation data generated with an analytical galaxy model.

Fortunately, launches of next-generation astrometry satellites are now approaching: *Gaia* (Perryman et al. 2001), *Nano-JASMINE* (Japan Astrometry Satellite Mission for INfrared Exploration, Gouda 2011) and *JMAPS* (Joint Milli-Arcsecond Pathfinder Survey, Gaume et al. 2009). These satellites will provide astrometric information of Galactic stars with unprecedented precisions. Therefore, it is worth performing a feasibility study of determining the LDMD with data provided by them. We study the dependence of a determined LDMD on a sampling region and observational errors such as parallaxes, proper motions and line-of-sight velocities (LOSVs). Our second aim is to evaluate required sample size and observational precisions to determine the LDMD with accuracy.

The basic concept of the MA method is described in Sect. 2. Our galaxy model for the mock observations and how to create the mock data are explained in Sect. 3 and 4, respectively. A Markov chain Monte Carlo (MCMC) technique combined with the MA method is explained in Sect. 5. Our results are shown in Sect. 6. Discussion and our conclusions are presented in Sect. 7 and Sect. 8, respectively. Since Sect. 2 and 5 basically follow the same course of action as G12, readers who are already familiar with the MA method or only intended in our results may prefer to skip these sections.

2. The MA method

Here we explain procedures to derive the LDMD with the MA method; however, we recommend that readers refer to G11 and G12 for the original idea.

2.1. Basic equations and deduced galaxy models for the MA method

To begin with, we assume that the Galaxy can be modeled as a superposition of multiple visible components, such as stellar and gaseous disks, stellar halo, and a dark component, i.e., $\rho_{\rm tot} \equiv \sum \rho_i + \rho_{\rm dm}$, where ρ_i represents *mass* density of the i-th visible component, and $\rho_{\rm tot}$ and $\rho_{\rm dm}$ are the total and DM mass density, respectively. Next, the MA method introduces only three assumptions:

(1) the system is in equilibrium,
(2) a "tilt" term in the Jeans equation is negligible,
(3) the DM density is constant in a region we consider.

G11 have confirmed that all of these assumptions hold in an N-body simulation of a barred spiral galaxy.

---

[3] Some studies are, however, inconsistent with the result of the oblate halo, preferring an approximately spherical halo (e.g., Ibata et al. 2001; Fellhauer et al. 2006) and a prolate halo (e.g., Helmi 2004).

[4] Moni Bidin et al. (2012) proposed absence of DM around the sun from their analysis of thick disk stars. However, Bovy & Tremaine (2012) claimed that this result significantly underestimates the LDMD because of a false assumption.

From the assumption (1), the i-th component satisfies the Jeans equation. Considering the direction perpendicular to the Galactic disk (z-axis), the Jeans equation is described as

$$\frac{1}{R}\frac{\partial}{\partial R}\left(R\nu_i\overline{v_{R,i}v_{z,i}}\right)+\frac{\partial}{\partial z}\left(\nu_i\sigma_{z,i}^2\right)+\nu_i\frac{\partial\Phi}{\partial z}=0, \tag{1}$$

where ν_i is density of the i-th component under the total gravitational potential, Φ, and the over-line means the averaged value, and σ_z is vertical velocity dispersion. The first term is often called the tilt term. From the assumption (2), Eq. (1) ignoring the tilt term can be reduced to

$$\sigma_{z,i}^2\frac{\partial\nu_i}{\partial z}+\nu_i\left(\frac{\partial\sigma_{z,i}^2}{\partial z}+\frac{\partial\Phi}{\partial z}\right)=0. \tag{2}$$

Integrating this equation, one can obtain a density profile of the i-th population as

$$\frac{\nu_i(z)}{\nu_i(0)}=\frac{\sigma_{z,i}^2(0)}{\sigma_{z,i}^2(z)}\exp\left(-\int_0^z\frac{1}{\sigma_{z,i}^2(z')}\frac{\mathrm{d}\Phi}{\mathrm{d}z'}\mathrm{d}z'\right). \tag{3}$$

$\sigma_{z,i}(0)$ are given as parameters, whereas the profiles of $\sigma_{z,i}(z)$ must be assumed to solve this equation.[5] G11 introduced parametrized runs of $\sigma_{z,i}(z)$, and G12 assumed isothermality for all components of the galaxy model. Following G12, we also assume that the model components are isothermal; however we discuss the influence of different $\sigma_{z,i}(z)$ profiles on the calculation in Appendix A. With the isothermal assumption, Eq. (3) becomes

$$\rho_i(z)=\rho_i(0)\frac{\sigma_{z,i}^2(0)}{\sigma_{z,i}^2(z)}\exp\left(-\frac{\Phi(z)}{\sigma_{z,i}^2(0)}\right). \tag{4}$$

Here, ρ_i is mass density: $\rho_i=\nu_i m_i$, where m_i is the mass-to-light ratio of the i-th population. $\rho_i(0)$ are given as parameters. Finally, one can describe the profile of the total observable density as $\rho_{\rm s}(z)=\sum_i\rho_i(z)$. Then, the total matter density is $\rho_{\rm tot}(z)=\rho_{\rm s}(z)+\rho_{\rm dm}$ from the assumption (3). In addition, the total surface density of the observable matters is derived as

$$\Sigma_{\rm s}(z)=2\int_0^z\rho_{\rm s}(z')dz'. \tag{5}$$

Next, $\rho_{\rm tot}$ is connected to the total gravitational potential, Φ, via the Poisson equation:

$$4\pi G\rho_{\rm tot}=\frac{\partial^2\Phi}{\partial z^2}+\frac{1}{R}\frac{\partial V_c^2(R)}{\partial R}. \tag{6}$$

This is transformed to

$$\frac{\partial^2\Phi}{\partial z^2}=4\pi G\left(\rho_{\rm s}(z)+\rho_{\rm dm}+\frac{1}{4\pi GR}\frac{\partial V_c^2(R)}{\partial R}\right). \tag{7}$$

This equation implies that the radial gradient of circular velocity, $\frac{\partial V_c^2}{\partial R}$, causes a pseudo-mass which can be either positive or negative. However, if the z-dependence of this term is ignored, it can be simply subtracted from the "effective" LDMD, $\rho_{\rm eff}\equiv\rho_{\rm dm}+\frac{1}{4\pi GR}\frac{\partial V_c^2(R)}{\partial R}$, finally. Although Bovy & Tremaine (2012) pointed out that neglecting the z-dependence of $\frac{\partial V_c^2}{\partial R}$ can lead to underestimation of the LDMD, they also evaluated the underestimation as being only a tiny fraction of the matter density at low z where the thin disk components are dominant. Additionally, this term is observationally accessible via the Oort constants.[6] Accordingly, we exclude the term of circular velocity gradient: Eq. (7) simply becomes

$$\frac{\partial^2\Phi}{\partial z^2}=4\pi G\left(\rho_{\rm s}(z)+\rho_{\rm dm}\right). \tag{8}$$

One can now compute the potential of the model galaxy, Φ, by numerical integration of Eq. (4) and (8) with a given parameter set of $\rho_i(0)$, $\sigma_{z,i}(0)$ and $\rho_{\rm dm}$ and boundary conditions of $\Phi=\frac{\partial\Phi}{\partial z}=0$ at $z=0$. The total number of the parameters is, therefore, $2n+1$, where n is the number of visible components in the galaxy model. In this paper, we refer to the computed potential, Φ, as the "deduced model".

2.2. A tracer population

The reliability of a trial parameter set used in the above computation of Φ must be evaluated by comparing with observations. To this end, the MA method prepares an observed sample of "tracer" population stars. The tracer stars must share the same kinematic state. The preferred tracer stars are considered to be old (well-mixed), bright (observationally precise and accurate) and large in number (statistically reliable).

Let us now assume that a sample of tracer stars is available, and we obtain density and velocity dispersion profiles, $\nu_{\rm trac}^{\rm obs}(z)$ and $\sigma_{z,{\rm trac}}^{\rm obs}(z)$, in a range from $z_{\rm min}$ to $z_{\rm max}$. Substituting $\sigma_{z,{\rm trac}}^{\rm obs}(z)$ for $\sigma_{z,i}$ in Eq. (3), one can *deduce* a fall-off of the tracer density profile under the modeled potential, Φ, as

$$\frac{\nu_{\rm trac}^{\rm ded}(z)}{\nu_{\rm trac}^{\rm ded}(z_{\rm min})}=\frac{\sigma_{z,{\rm trac}}^{2\ {\rm obs}}(z_{\rm min})}{\sigma_{z,{\rm trac}}^{2\ {\rm obs}}(z)}\exp\left(-\int_{z_{\rm min}}^z\frac{1}{\sigma_{z,{\rm trac}}^{2\ {\rm obs}}(z')}\frac{\mathrm{d}\Phi}{\mathrm{d}z'}\mathrm{d}z'\right). \tag{9}$$

This deduced density fall-off can be compared with the observed fall-off, $\nu_{\rm trac}^{\rm obs}(z)/\nu_{\rm trac}^{\rm obs}(z_{\rm min})$, and goodness-of-fit between them is calculated to estimate the values of the model parameters. Although our study uses a single tracer population, the MA method does not necessarily require only a single tracer, but multiple tracers can also be used.

Since the MA method usually introduces a large number of parameters, an MCMC technique should be applied to explore the vast parameter space (see Sect. 5). Then, as a result, probability distribution functions (PDFs) and their degrees of uncertainties are obtained for all of the model parameters.

3. An assumed Galaxy model for mock observations

In this paper, we do not make use of observational data or intend to determine the LDMD in the real Galaxy. Instead, our study performs mock observations of a tracer sample using an analytical model, and aims to assess the capability of the MA method by deriving an LDMD assumed arbitrarily. To this end, we prepare an *assumed* galaxy model for the purpose of creating the mock tracer data.

---

[5] It is impossible to observe $\sigma_{z,i}(z)$ of all components up to high z, therefore we have to assume their runs. We consider the situation where only a velocity dispersion profile of a tracer population is available.

[6] Bovy et al. (2012a) estimated that the contribution of this term to the local density is only $0.0002^{+0.0002}_{-0.0025}$ $\mathrm{M}_\odot$ pc^{-3}, and G11 estimated -0.0033 ± 0.0050 $\mathrm{M}_\odot$ pc^{-3} from observations of Mignard (2000) and Branham (2010).

First, we assume that density profiles of all visible components are represented as $\rho_i^{\rm ass} \propto {\rm sech}^2\left(z/(2h_i)\right)$ although this may not be suitable for gas or stellar halo components. Then, the total density structure perpendicular to the disk plane is

$$\rho_{\rm tot}^{\rm ass}(z) = \sum_i \rho_i^{\rm ass}(0){\rm sech}^2\left(\frac{z}{2h_i}\right) + \rho_{\rm dm}, \tag{10}$$

where $\rho_i^{\rm ass}(0)$, h_i and $\rho_{\rm dm}$ are set arbitrarily. $\rho_{\rm dm}$ is a constant according to the assumption (2). By integrating the Poisson equation with the boundary condition of $\frac{\partial\Phi^{\rm ass}}{\partial z} = 0$ at $z = 0$, the differential of this galactic potential is calculated analytically:

$$\frac{{\rm d}\Phi^{\rm ass}}{{\rm d}z} = 4\pi G\left[2\sum_i h_i\rho_i^{\rm ass}(0)\tanh\left(\frac{z}{2h_i}\right) + \rho_{\rm dm}z\right]. \tag{11}$$

This is related to the total surface density as $\frac{{\rm d}\Phi^{\rm ass}}{{\rm d}z} = 4\pi G\Sigma^{\rm ass}(z)$, and surface density of all observable matters is $\Sigma_{\rm s}^{\rm ass}(z) = 2\sum_i h_i\rho_i^{\rm ass}(0)\tanh\left(z/(2h_i)\right)$. Next, we may integrate Eq. (2) from arbitrary z to $z = +\infty$. Since $\rho_i^{\rm ass}(z) \to 0$ as $z \to +\infty$,

$$\sigma_{z,i}^2(z) = \frac{1}{\rho_i^{\rm ass}}\int_z^\infty \rho_i^{\rm ass}\frac{{\rm d}\Phi^{\rm ass}}{{\rm d}z'}{\rm d}z'. \tag{12}$$

Substituting Eq. (11) and $z = 0$ in this equation, we can compute $\sigma_{z,i}(0)$ when a set of $\rho_i^{\rm ass}(0)$, h_i and $\rho_{\rm dm}$ are given. We refer to this galaxy model as an "assumed model". In this study, we presume that this assumed model represents the real Galaxy.

Following Garbari et al., we assume that the model consists of fifteen visible components with $\rho_i^{\rm ass}(0)$ listed in Table 1 that are taken from observations of Flynn et al. (2006). The LDMD is set to $\rho_{\rm dm} = 0.01$ $M_\odot$ pc^{-3}. In addition, we determine h_i as follows: In the calculation above, $\sigma_{z,i}(0)$ are the output, and h_i are the input parameters; however, $\sigma_{z,i}(0)$ can be determined by observations of nearby stars and gas, whereas h_i are poorly known. Therefore, it is preferable to search for a set of h_i which matches $\sigma_{z,i}(0)$ computed by Eq. (12) to the observed values. Accordingly, we employ an MCMC method to find such a set of h_i. The result of the set of h_i is shown in the last column of Table 1.[7] After h_i are obtained, we recompute $\sigma_{z,i}(0)$ by Eq. (12) with the set of h_i. These are shown in the fifth column, indicating excellent agreement with the observations (the fourth column). We adopt $\rho_i^{\rm ass}(0)$ in the third column and $\sigma_{z,i}(0)$ in the fifth column for the assumed model described by Eq. (10).

The total observable surface density of the assumed model is $\Sigma_{\rm s}^{\rm ass}|_{z=\infty} = 49.6$ $M_\odot$ pc^{-2}, this is in excellent agreement with the observed value of $\Sigma_{\rm s}^{\rm obs} = 49.4 \pm 4.6$ $M_\odot$ pc^{-2} by Flynn et al. (2006); however, it should be noted that h_i seem to be somewhat shorter than observed scale heights of $\simeq 300$ pc for Galactic thin disk components (e.g., Gilmore & Reid 1983; Binney & Merrifield 1998; Bovy et al. 2012b,d).

4. The mock data

As mentioned in Sect. 2.2, the MA method needs density fall-off and velocity dispersion profiles of an observed tracer population. Accordingly, we create tracer stars that are dynamically consistent with the assumed galaxy model in Sect. 3. We assign three-dimensional positions and velocities in the Cartesian coordinates, (x, y, z, v_x, v_y, v_z), to the tracer stars. In this model, the sun is presumed to be located at $(x, y, z) = (0, 0, 0)$ and at rest.

As well as the model components, we assume the tracer density profile to be

$$\nu_{\rm trac}(z) = \nu_{\rm trac}(0){\rm sech}^2\left(\frac{z}{2h_{\rm trac}}\right), \tag{13}$$

where $\nu_{\rm trac}(0)$ is a constant, and we set $h_{\rm trac} = 200$ pc. We assume that the tracer stars are uniformly distributed on xy-plane at a height above the plane: $\nu_{\rm trac}$ depends only on z. Thus, we can place tracer stars at random in spatial coordinates according to Eq. (13).

The vertical velocity dispersion profile can be calculated by Eq. (12) using the assumed model:

$$\sigma_{z,{\rm trac}}^2(z) = \frac{1}{\nu_{\rm trac}}\int_z^\infty \nu_{\rm trac}\frac{{\rm d}\Phi^{\rm ass}}{{\rm d}z'}{\rm d}z'. \tag{14}$$

Motions of the tracers in the Galactic radial (x-) and azimuthal (y-) directions can be taken from the observational fitting functions of Bond et al. (2010). We assume that there are no meridional motions: $\overline{v_{x,{\rm trac}}} = 0$, and velocity dispersion in the radial direction is

$$\sigma_{x,{\rm trac}}(z) = 40 + 5\left(\frac{z}{\rm kpc}\right)^{1.5} {\rm km\ s^{-1}}. \tag{15}$$

Mean azimuthal velocity with respect to the sun decreases with increasing z,

$$\overline{v_{y,{\rm trac}}}(z) = -19.2\left(\frac{z}{\rm kpc}\right)^{1.25} {\rm km\ s^{-1}}. \tag{16}$$

This is often referred to as asymmetric drift (e.g., Binney & Merrifield 1998; Binney & Tremaine 2008). Also, the azimuthal velocity dispersion profile is given as

$$\sigma_{y,{\rm trac}}(z) = 30 + 3.0\left(\frac{z}{\rm kpc}\right)^{2.0} {\rm km\ s^{-1}}. \tag{17}$$

Assuming Gaussian velocity distributions with the dispersions above, we can assign a velocity vector to each tracer star. However, it should be noted that velocity distributions may not be Gaussian in the real Galaxy. In addition, the observations of Bond et al. (2010) are for blue stars, whereas the tracer population should be old (red) stars.

Now that we can assign (x, y, z, v_x, v_y, v_z) to the tracer stars according to the equations and assumptions above, the positions and the velocities are converted to the spherical coordinates of $(d, \theta, \phi, v_{\rm los}, v_\theta, v_\phi)$ which are centered at the sun, where d is distance from the sun, and $v_{\rm los}$ is LOSV. We apply mock observational errors to the stellar positions and velocities (see Sect. 6), then we turn the *errored* positions and velocities back to the Cartesian coordinates $(x', y', z', v_x', v_y', v_z')$. Next, we pick out stars contained in a certain sampling region, then we divide the sample stars into z-bins; the number of the bins is set to $n_{\rm bin} = 10$ in this study. The z-bins have the equal widths of $(z_{\rm max} - z_{\rm min})/n_{\rm bin}$, which are centered at z_j. Finally, we obtain profiles of $\nu_{\rm trac}^{\rm obs}(z_j)$ and $\sigma_{z,{\rm trac}}^{\rm obs}(z_j)$ affected by the mock errors. We apply the MA method to these errored profiles and examine the influence of the observational errors, sample sizes and sampling regions on determination of the LDMD. We hereafter set $z_{\rm min} = 0.2$ kpc and $z_{\rm max} = 1.2$ kpc unless otherwise stated.

---

[7] This MCMC calculation can also be applied to the case in which $\rho_{\rm dm}$ is taken as another parameter. In this case, the MCMC can estimate $\rho_{\rm dm}$ directly. However, the result prefers an extremely low LDMD, $\rho_{\rm dm} \simeq 0$, in such a case. This may imply that the density profiles of ${\rm sech}^2\left(z/(2h_i)\right)$ cannot be applied to all components in the Galaxy.

Table 1. Parameters used in the assumed galaxy model. This model assumes the fifteen visible components shown in the second column, following Garbari et al. in which their disk mass model is taken from Flynn et al. (2006, the third and fourth columns). In this model, we adopt $\rho_{\rm dm} = 0.01$ M$_\odot$ pc^{-3} and derive h_i (the last column) with MCMC calculation. Using the set of h_i, the fifth column is recalculated by Eq. (12). Our assumed model of Eq. (10) uses the third and sixth columns. The uncertainties on $\sigma_{z,i}(0)$ are set to be the same as Garbari et al.

#	Component	$\rho_i^{\rm ass}(0)$ [M$_\odot$ pc^{-3}] (observation)	$\sigma_{z,i}(0)$ [km s^{-1}] (observation)	$\sigma_{z,i}(0)$ [km s^{-1}] (MCMC)	h_i [pc] (MCMC)
1	H_2	0.021	4.0	3.80±1.0	32.4
2	HI(1)	0.016	7.0	7.00±1.0	63.4
3	HI(2)	0.012	9.0	9.02±1.0	84.7
4	Warm gas	0.0009	40.0	40.1±2.0	564
5	Giants	0.0006	20.0	20.0±2.0	224
6	$M_v < 2.5$	0.0031	7.5	7.56±2.0	69.2
7	$2.5 < M_v < 3.0$	0.0015	10.5	10.7±2.0	103
8	$3.0 < M_v < 4.0$	0.0020	14.0	14.1±2.0	144
9	$4.0 < M_v < 5.0$	0.0022	18.0	18.1±2.0	197
10	$5.0 < M_v < 8.0$	0.007	18.5	18.5±2.0	203
11	$M_v > 8.0$	0.0135	18.5	18.4±2.0	201
12	White dwarfs	0.006	20.0	20.1±5.0	226
13	Brown dwarfs	0.002	20.0	20.0±5.0	224
14	Thick disk	0.0035	37.0	37.7±5.0	519
15	Stellar halo	0.0001	100.0	99.8±10.0	1891

5. The MCMC method

The MA method is combined with the MCMC technique to explore the vast parameter space. We introduce fitting errors of the tracer density bins as

$$\chi_v^2 = \frac{1}{n_{\rm bin}} \sum_{j=1}^{n_{\rm bin}} \left[\frac{v_{\rm trac}^{\rm ded}(z_j)/v_{\rm trac}^{\rm ded}(z_{\rm min}) - v_{\rm trac}^{\rm obs}(z_j)/v_{\rm trac}^{\rm obs}(z_{\rm min})}{\varepsilon v_{\rm trac}^{\rm obs}(z_j)/v_{\rm trac}^{\rm obs}(z_{\rm min})} \right]^2, \tag{18}$$

and an error of the surface density of all observable matters as

$$\chi_\Sigma^2 = \left[\frac{\Sigma_s^{\rm ass}(z_{\rm max}) - \Sigma_s(z_{\rm max})}{\varepsilon \Sigma_s(z_{\rm max})} \right]^2, \tag{19}$$

where ε is a constant that mimics uncertainty in actual observations (e.g., stellar mass estimation error). Throughout this study, we set $\varepsilon = 0.1$. Although the setting of ε is arbitrary, generally the result does not depend too much on ε. $\Sigma_s^{\rm ass}(z_{\rm max})$ is 47.1 M$_\odot$ pc^{-2} in the assumed model. We define the total error of the fittings to be

$$\chi_{\rm tot}^2 = (1-w)\chi_v^2 + w\chi_\Sigma^2, \tag{20}$$

where w is a weight of the surface density error; $0 \leq w \leq 1$. A larger w means that the surface density fitting has stronger constraint in determining the best-fit parameters.

We use a Gaussian function as our likelihood function: $P \equiv \exp\left(-\chi_{\rm tot}^2\right)$. A MCMC chain computes the likelihood at each step and decides whether a proposed next step is accepted or rejected according to a ratio of the likelihoods (e.g., Gregory 2010). We use a Metropolis-Hasting algorithm for our sampling scheme and run the MCMC chains of 50,000 steps: however, the first 5,000 steps are excluded as a burn-in period.

Parameter ranges surveyed in our study are from 0 to 0.2 M$_\odot$ pc^{-3} for $\rho_{\rm dm}$, ±10 % and ±25 % for $\rho_i^{\rm ass}(0)$ of stellar and gas components, respectively. The ranges for $\sigma_{z,i}(0)$ are listed in Table 1, and are much wider than actual observational uncertainties (Holmberg & Flynn 2000). The medians of resultant PDFs are used as the best fit values. The 90 % confidence levels (intervals between the 5th and 95th percentiles) are used as ranges of uncertainties of the calculation.

6. Results

6.1. Application to the analytical solutions

Before adapting the MA method to the mock observation data, we directly substitute the analytical velocity dispersion profile of Eq. (14) in Eq. (9) and run the MCMC by fitting with the analytical density of Eq. (13). In such a case, we can investigate intrinsic systematic biases of the MA method.

To begin with, we study the case of $w = 0$: no constraint by the surface density. The result is shown in Figure 1. We can see that the LDMD is accurately determined; besides, the local and surface observable densities obtained are accurate enough to be within the 90 % confidence levels. From this result, we expect that the isothermality assumed in Eq. (3) for the deduced model does not lead to significant systematic biases (see also Appendix A) and that the MA method would be capable of determining the LDMD accurately if there are no observational errors and a sample size is large enough. We find, however, that $\rho_i(0)$ and $\sigma_{z,i}(0)$ of each component are largely degenerate with one another and not particularly well constrained.

6.1.1. The surface density constraint in the MCMC

In the right panel of the Figure 1, the shape of the PDF is inclined from the upper left to the lower right. This implies that $\rho_{\rm dm}$ and $\Sigma_{\rm s}$ have a correlation. Therefore, it may be expected that if $\Sigma_{\rm s}$ can be determined more precisely, the error range of $\rho_{\rm dm}$ can become narrower: the constraint on $\Sigma_{\rm s}$ in the MCMC computation may help to suppress the uncertainty of $\rho_{\rm dm}$.

Figure 2 shows our results in the cases of $w = 0.1$, 0.5 and 0.7. Contrary to the expectation above, the error ranges of $\rho_{\rm dm}$

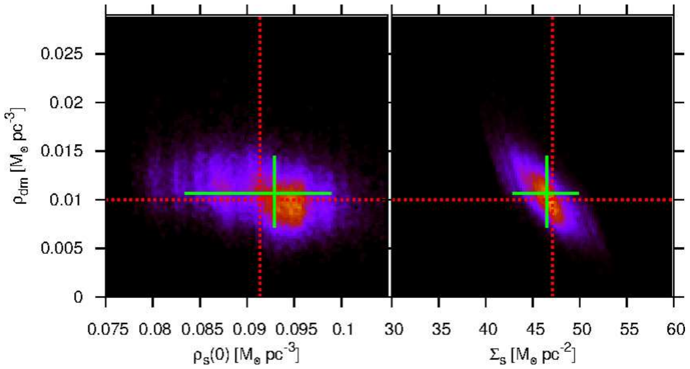

Fig. 1. PDFs of LDMD, local and surface densities of the all visible matters. Here, we adopt the analytical solutions of the tracer density and velocity dispersion profiles and $w = 0$ in the calculation. The left and right panels illustrate the PDFs of LDMD v.s. local and surface densities of the visible matters, respectively. The brighter regions mean higher probabilities. The green solid lines indicate the ranges of the 90 % confidence levels, and their intersection points are the medians. The red dotted lines indicate the true values in the assumed model.

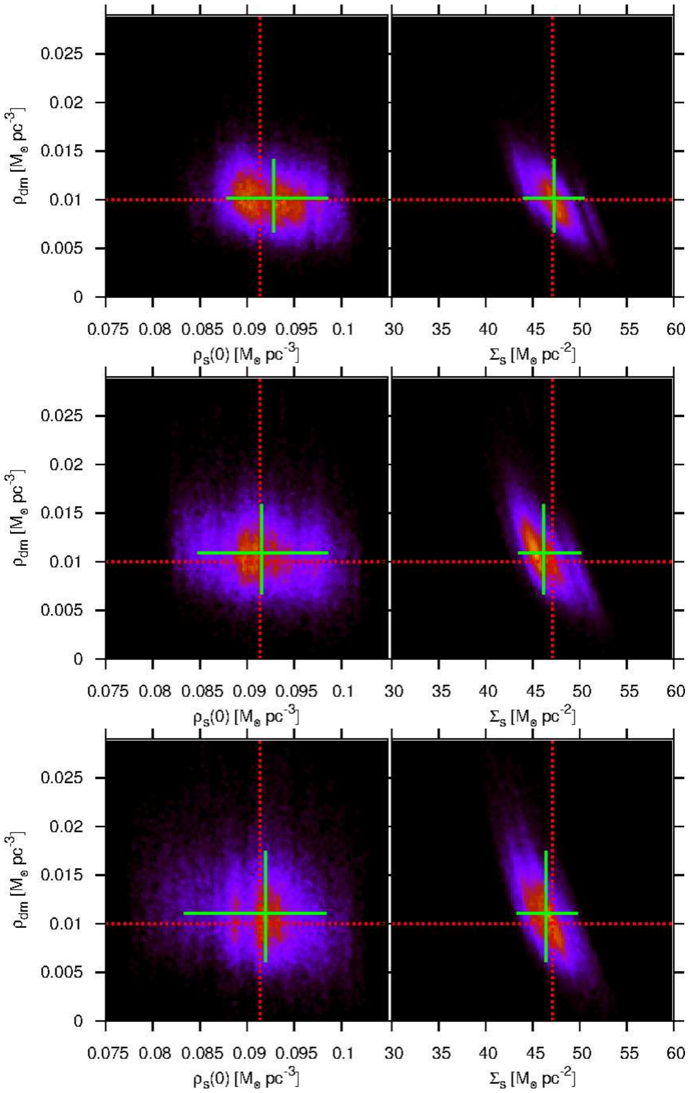

Fig. 2. Same as in Figure 1, but adopting $w = 0.1$, 0.5 and 0.7 from top to bottom.

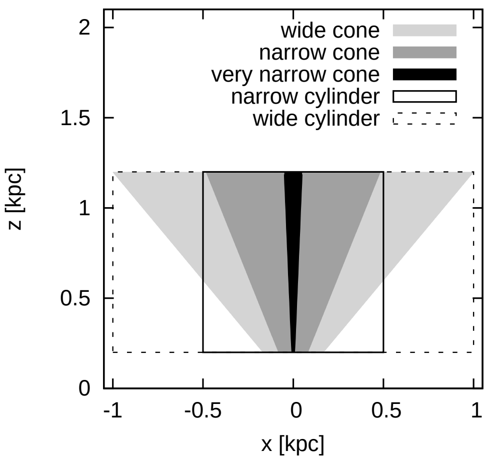

Fig. 3. Sampling regions for the tracer stars. These are axisymmetric.

widen as w increases; in addition, the inclinations of the PDFs in the right panels become steep. This is due to the constraint on the tracer density fall-off becoming weaker as w becomes larger; therefore, too large w should not be used. The best-fit values of $\rho_{\rm dm}$, $\Sigma_{\rm s}$ and $\rho_{\rm s}(0)$ are little affected by w. The PDFs in the case of $w = 0.1$ differ very little from those in the case of $w = 0$ (Figure 1) although the error range of $\rho_{\rm s}(0)$ is somewhat narrower. Hence, we consider that the constraint on $\Sigma_{\rm s}$ in the MCMC may not necessarily make the determination better. Following G12, we hereafter set $w = 0.1$.[8]

6.2. Application to the mock observation data

We generate the mock tracer population following the procedure described in Sect. 4 and *observe* the sample stars contained in various regions. We test five sampling regions: “narrow cone”, “very narrow cone”, “wide cone”, “narrow cylinder” and “wide cylinder”. These cone regions are directed to the z-axis ($\theta = 0$) and contain stars within $\theta < 22^\circ$ (narrow), 2.4° (very narrow) and 40° (wide). The cylinders cover the regions of $R = \sqrt{x^2 + y^2} < 0.5$ kpc (narrow) and < 1.0 kpc (wide). Figure 3 delineates these sampling regions.

6.2.1. Sample sizes

If tracer stars are insufficient in their sample size, statistical uncertainty may lead to an ill-determined LDMD. Here we investigate the sample size required to determine the LDMD precisely. For this reason, we assume no observational errors here. In this case, since our tracer model assumes the horizontally uniform distribution and kinematics, the widths of the sampling regions do not change the results. The cylinder sampling region contains more stars at lower z since the stellar density decreases with increasing z, whereas the cone region can cover wider areas at higher z. Therefore, if the sample size is fixed, samples in the cylinder and the cone can be statistically reliable in low and high z regions, respectively.

We perform the calculations using the MA method with tracer samples of 1,500–24,000 stars. Our results in the cases of

---

[8] In G12, $w = 0.1$ was adopted although they did not introduce the parameter explicitly: they used nine bins of a tracer density profile and a surface density.

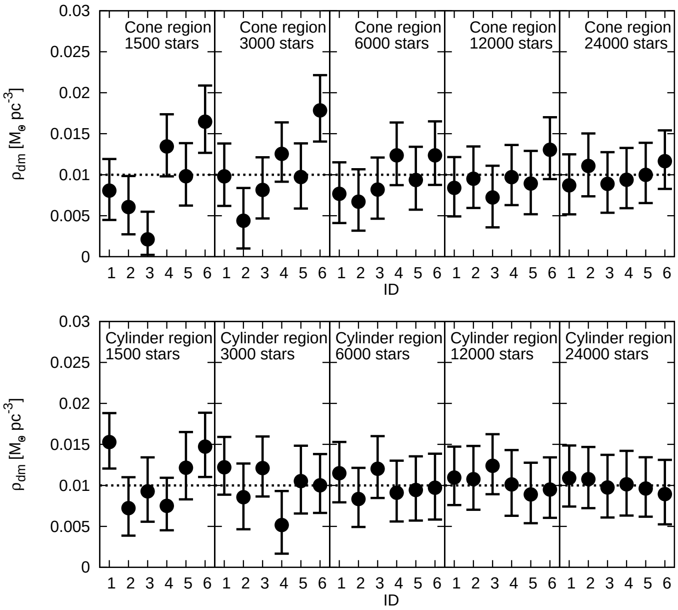

Fig. 4. Results of derived LDMDs with various sample sizes. For each sample size, we performed the same computation six times with samples generated by different random seeds. The points and the error bars indicate the best-fit values and the 90 % confidence levels, respectively. The horizontal dotted line indicates the true LDMD, $\rho_{\rm dm} = 0.01$ M$_\odot$ pc^{-3}.

cone and cylinder regions are shown in Figure 4. For each case, we run the same computation six times using different random seeds in generating the samples. In both cases of the cone and cylinder sampling regions, the resultant LDMDs with $\leq 3,000$ stars are not precise, and the true LDMDs are often out of the error ranges. The samples of $\geq 6,000$ stars seem sufficient for determining the LDMD within the errors in all runs. Therefore we consider that the minimum sample size to precisely determine the LDMD would be 6,000 stars. The scatter of the LDMDs seems slightly smaller in the case of the cylinder region than in the case of the cone region, implying that statistics in lower z regions are more important. To suppress the statistical uncertainty, we set the tracer sample size to be 24,000 stars hereafter, unless otherwise stated.

6.2.2. Distance errors

Astrometric observations usually measure stellar parallaxes and proper motions on the celestial sphere. The parallax measurements determine trigonometric distances to the stars. Using the distances measured, the proper motion measurements can determine transverse velocities of the stars. One of great advantages of astrometric observations is that systematic errors are generally very small (e.g., Perryman et al. 1997; de Bruijne et al. 2005; Perryman 2012). For this reason, we examine the influence of distance-dependent random errors of parallax measurements. We assume no systematic errors —in other words, the mock observations are accurate but imprecise— and no errors on stellar position measurements (θ and ϕ); besides, we do not take into account dust extinction or binary stars.

To begin with, we simply analyze how precisions of astrometric measurements varies with distances of stars. Let ϖ and μ_θ be parallax and proper motion in the θ-direction of a star. Apart from bright sources, uncertainty of the parallax is thought to be dominated by photon statistics to determine an image centroid (e.g., de Bruijne et al. 2005). In this case, the parallax error, ε_ϖ, varies with the observed stellar flux, f, as $\varepsilon_\varpi \propto 1/\sqrt{f}$. Since $f \propto d^{-2}$, $\varepsilon_\varpi \propto d$. On the other hand, if the source is bright enough to obtain a sufficient number of photons and the photons do not saturate the image, the parallax error is expected to be independent from the distance. Accordingly, we can formulate the parallax measurement error as $\varepsilon_\varpi \propto d^\alpha$, where $\alpha = 0$ or 1. Besides, the parallax itself decreases as distance increases: $\varpi = 1/d$. This means that the fractional parallax error depends on the distance as $\varepsilon_\varpi/\varpi \propto d^{\alpha+1}$ (e.g., Bailer-Jones 2009). Since we can equate this fractional parallax error with the fractional distance error (FDE), we formalize as

$$\varepsilon_{\rm FDE} = A\left(\frac{d}{\rm kpc}\right)^{\alpha+1}, \qquad (21)$$

where A is a parameter which corresponds to the precisions of parallax measurements at $d = 1$ kpc in milliarcsecond (mas) units. We apply this FDE with Gaussian probability distributions the dispersion of which is $\varepsilon_{\rm FDE}$ to the mock tracer stars. In addition, since astrometric measurements determine transverse velocities as $v_\theta = d \times \mu_\theta$, transverse velocities are also subject to the distance error as $v'_\theta = v_\theta \frac{d'}{d}$, where v'_θ and d' are errored transverse velocities and distances. However, it should be noted that the formulation above may be simplistic. α would not be a constant but varies with d in actual observations: when $\alpha = 1$, the parallax uncertainties cannot be zero at $d = 0$ but are limited to calibration errors and/or instrument stability at a certain distance. Moreover, in the cases of conical sampling regions with fixed angles, observations may suffer from Lutz-Kelker bias (Lutz & Kelker 1973; Binney & Merrifield 1998, see also Smith 2003). In this subsection, we examine the influence on determining the LDMD by the distance error alone; therefore, we ignore the errors on proper motions and LOSVs here.

Figure 5 shows our results of LDMDs determined in cases of various A, α and the sampling regions. Our results obviously demonstrate that the distance errors cause systematic overestimation of $\rho_{\rm dm}$, regardless of the sampling regions. $\rho_{\rm dm}$ is significantly overestimated beyond the error ranges when $A \geq 0.3$ in all cases except the wide cylinder with $\alpha = 1$. Therefore, the parallax measurement precisions must be $A \leq 0.1$ which corresponds to ≤ 0.1 mas at $d = 1$ kpc. Only in the case of the wide cylinder with $\alpha = 1$, the required accuracy seems to be 0.05 mas. The magnitudes of the overestimation seem to depend only weakly on α and the shapes of the sampling regions.

The overestimation shown in Figure 5 is attributed to changes in density and velocity dispersion profiles of the tracer due to the distance errors. In Figure 6, we show how the distance errors deteriorate the reproducibility of these profiles. The density fall-offs are similarly affected in both the cone and the cylinder sampling regions; however, the velocity dispersion profiles are more significantly changed in the cases of the cylinders. In the top panel, the velocity dispersion profile is hardly changed in the case of the very narrow cone; however, the LDMD is significantly overestimated even in this case (Figure 5). Therefore, it can be said that the overestimation can be caused solely by the change of density fall-off; however, it can also be caused solely by the change of velocity dispersion (see Sect. 6.2.4). The changes of velocity dispersion profiles are more serious in the cases of cylinders than in the cones. This is due to inclusion among tracer stars in the cylinder regions stars whose θ are large in low z regions. On such stars, their transverse velocities have more information about v_z than their LOSVs.

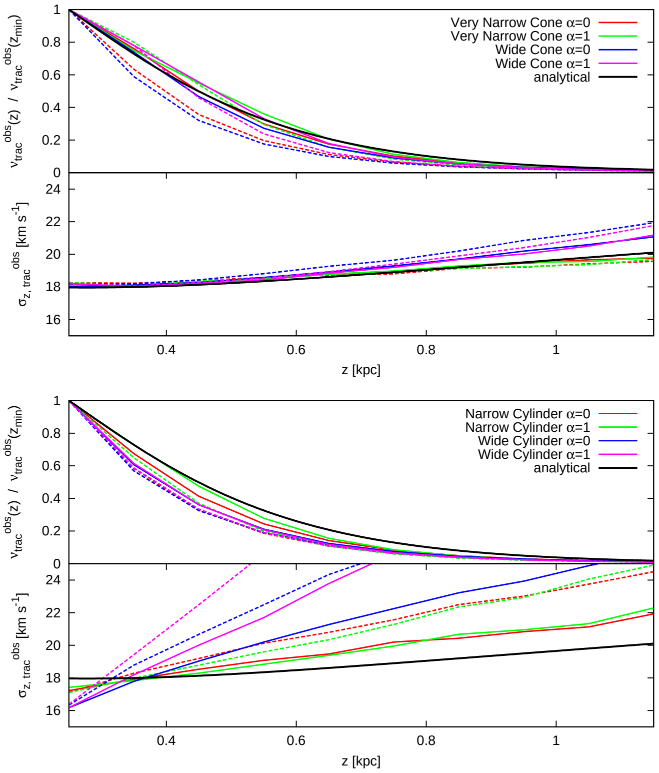

Fig. 6. Changes of density fall-off and vertical velocity dispersion profiles of the tracers. Here we take into account the distance errors only. The line colors indicate results of different sampling regions and α. The solid and dashed lines indicate results of $A = 0.3$ and 0.5, respectively. Here we used mock data of one million tracer stars in all cases.

6.2.3. Proper motion errors

Proper motion uncertainties also varies with distance in the same way as parallaxes, we therefore formalize the proper motion error in the θ-direction, ε_μ, as

$$\varepsilon_\mu = B\left(\frac{d}{\mathrm{kpc}}\right)^{\alpha} \text{mas yr}^{-1}. \tag{22}$$

where B is a parameter that corresponds to the precisions of proper motion measurements at $d = 1$ kpc in the unit of mas yr^{-1}, α is the same as in Eq. (21). We assume Gaussian errors with the dispersion of ε_μ and add the errors to the true proper motions. Errored transverse velocities are $v'_\theta = d' \times \mu'_\theta$, where μ'_θ is the errored proper motion.

In most cases in Figure 5, the LDMD is overestimated by the distance errors when $A \geq 0.3$; therefore, we here set $A = 0.1$ in all cases. Figure 7 shows our results of adopting various B, α and sampling regions. In the figure, the overestimation of LDMD is little seen where the cone sampling regions were used, even when $\beta = 3.0$. However, slight overestimation can be seen in use of the narrow cylindrical region when $B \geq 2.0$, and significant overestimation occurs in use of the wide cylinder region when $B \geq 1.0$. Again, this is because the cylindrical regions include stars with larger θ in lower z regions. Therefore, sampling in the cylindrical regions seems to have a risk of tracer kinematics becoming susceptible to the proper motion errors. Moreover, the magnitude of the overestimate seems to strongly depend on widths of the cylinders. Accordingly, we suggest that the shapes and widths of sampling regions be chosen carefully. The wide cylinder would be useful to gather more stars in low z regions; however, if precisions of proper motion measurements are insufficient in actual observations, the tracer sampling should be conducted in a conical region.

In Figure 8, we show comparison of changes of v_z caused by the errors on distances and the proper motions. In each three panels, the top left and top right panels indicate the influence of the errors on distances and proper motions, respectively. If there are no errors, the dots align diagonally across the panels. The scatter of the dots indicates significance of the error propagation to v_z. As seen in the figure, the changes of v_z by the proper motion errors appear less significant than those by the distance errors when $A = B$. This means that the distance errors are more crucial for determining the LDMD than the proper motion errors; moreover, the distance errors can also change the density profiles. The changes of v_z in the very narrow cone are much smaller than in the narrow cone, since contribution of the transverse velocities to v_z is $v_\theta \sin\theta$.

From Figure 7 and the discussion above, it may be expected that the proper motion measurements are not indispensable to derive the LDMD with the MA method if the sampling region is a cone. Distances to stars can be measured not only by astrometry but also by other observational means (e.g., photometric distances using a color-magnitude diagram). Hence, if the LDMD can be determined without proper motion measurements, it could be expected that we do not necessarily need astrometry. Accordingly, we also examine the cases of ignoring the proper motion measurements, where we set $\mu_\theta = 0$ for all tracer stars. Figure 9 shows our results in the cases of the very narrow and narrow cone sampling regions. It can be seen that the LDMD can be accurately determined without proper motions if the sampling region is the very narrow cone. On the other hand, in the case of the narrow cone, neglecting the proper motion measurements causes overestimation of the LDMD. These results do not change even if small distance errors with $A = 0.1$ are applied. Accordingly, it can be said that if tracer stars are observed in a sufficiently narrow conical region, proper motion measurements are not necessary. However, it may be difficult or impossible for such a narrow cone to contain a sufficient number of tracer stars; our result in Figure 4 suggests that the required sample size is 6,000 stars.

Data of a tracer population used in G12 was taken from a K star catalog of Kuijken & Gilmore (1989a) calibrated by $[\alpha/\mathrm{Fe}]$ distributions from *Hipparcos* (Kotoneva et al. 2002) and *Sloan Extension for Galactic Understanding and Exploration (SEGUE)*. Although their data do not seem to have proper motion measurements, since their sampling region is as narrow a cone as our very narrow cone, the high LDMD determined by G12 cannot be attributed to ignoring proper motions.

6.2.4. Line-of-sight velocity errors

Since we cannot obtain LOSVs of stars from astrometry alone and need independent spectroscopic observations, observational errors on LOSVs have no relation to the distance and proper motion errors. As well as the functional forms of the astrometric errors we introduced with Eq. (21) and (22), here we formalize the LOSV error as

$$\varepsilon_{losv} = C\left(\frac{d}{\mathrm{kpc}}\right)^{\beta} \text{km s}^{-1}, \tag{23}$$

where C and β are parameters. C corresponds to the LOSV uncertainties at $d = 1$ kpc in the unit of km s^{-1}. If quality of the spectroscopic observations is good enough, the LOSV precisions would be limited to wavelength resolutions and/or calibration errors of the observations: precision floors. In this case, the LOSV precisions can be assumed to be independent from distances to stars, which correspond to $\beta = 0$. Otherwise, we assume that the LOSV errors depend on signal-to-noise ratios of stars. If the signal-to-noise ratios are dominated by photon statistics, the LOSV errors can be ideally assumed to vary with stellar flux as $\varepsilon_{losv} \propto 1/\sqrt{f} \propto d$. This case corresponds to $\beta = 1$. However, the LOSV errors in actual observations are highly complicated (e.g., Katz et al. 2004; de Bruijne et al. 2005). We therefore examine cases in which $\beta = 0$–3 is adopted; in actual LOSV measurements, β seems to be in the range of 2–3 (e.g., Prusti 2012). However, again it should be noted that this formalization is simplistic. Even if it is the case of $\beta \geq 1$, the uncertainties are limited to the precision floors at $d \simeq 0$. Besides, the uncertainties depend on stellar populations. Because the LOSV measurements are independent from astrometric observations, we assume that there are no astrometric errors here: $A = B = 0$. In this case, the tracer density is not affected by the observational errors.

Figures 10 and 11 show our results of adopting the various C, β and sampling regions. In the cases of $\beta = 0$, the conical sampling regions overestimate the LDMD when $C > 3.0$ km s^{-1}, and the cylinders overestimate when $C > 5.0$ km s^{-1} in some runs. These values of C can be considered as the required precision floors of the LOSV measurements. Where $\beta = 1$, all of the sampling regions overestimate the LDMD when the errors are > 7.5 km s^{-1} at $d = 1$ kpc in some runs. Where $\beta = 2$ and 3 behavior of derived LDMDs is interesting; the LDMDs are underestimated. Where $\beta = 2$, the LOSV precision required to prevent significant underestimation is approximately 20 km s^{-1} at $d = 1$ kpc for the conical sampling regions and 30 km s^{-1} for the cylinders. Where $\beta = 3$, the precision required is approximately 10 km s^{-1} at $d = 1$ kpc for the conical sampling regions and 15 km s^{-1} for the cylinders.

Figure 12 shows changes of $\sigma^{\mathrm{obs}}_{z,\mathrm{trac}}(z)$ by the LOSV errors. The behavior of the velocity dispersion change is complicated. When $\beta = 0$, the very narrow cone and the wide cylinder are the most and the least susceptible to the LOSV errors, respectively; however, when $\beta \geq 2$, the very narrow cone and the wide cylinder are the least and the most susceptible, respectively. Figure 13 shows tracer density fall-offs *deduced* from Eq. (9) under the LOSV errors. All parameters of $\rho_i(0)$, $\sigma_{z,i}(0)$ and ρ_{dm} are set to the true values. This figure explains why the LOSV errors underestimate or overestimate the LDMD depending on β. Where $\beta = 0$ and 1, the MA method tends to predict thicker distributions of the tracer than in the case of excluding the LOSV errors; on the other hand, in the cases of $\beta = 2$ and 3, the MA method predicts thinner distributions. Generally, higher LDMDs make the tracer distribution thinner, while lower LDMDs yield thicker tracer distribution. Therefore, in the cases of $\beta = 0$ and 1, high LDMDs are required to match with the observed density fall-offs; in the cases of $\beta = 2$ and 3, low LDMDs are preferred.

7. Discussion

7.1. Required precisions and comparison with the previous studies

In Sect. 6.2, we generated mock data of tracer stars and applied the MA method to them. Sect. 6.2.1 is aimed at estimating the required sample size of the tracer. In both cases of the conical and cylindrical sampling regions, we find that the sample size required to determine the LDMD with accuracy is approximately 6,000 stars. G11 have used three tracer populations in their study, and their sample sizes are 139 K giants, 2026 A stars and 3080 F stars, respectively. Although the total number of their tracer stars is comparable to the required sample size we estimated, each of them is insufficient in number. Moreover, although the shortest sample of the K stars extends from $z = 0.2$ kpc to 0.7 kpc, the other two samples only cover the range of $z \leq 0.2$ kpc. Therefore, we suspect that the samples of G11 may lack sufficient tracer stars in high z regions. On the other hand, G12 used a single tracer population which consists of 2016 K stars used for the density fall-off and 580 K stars used for the velocity dispersion profile. The sample size of G12 is much shorter than the required sample size we estimated. Therefore, we also suspect that the LDMD of G12 may be imprecisely determined due to statistical uncertainty. Zhang et al. (2012) more recently derived the LDMD using their own method; their measurement of the LDMD was lower than that of Garbari et al. by a factor of 3 or 4. They used three tracer populations containing 3672, 1416 and 2001 K dwarfs. As well as G11, each tracer of Zhang et al. (2012) is insufficient in number although the total sample size is larger than the required sample size. However, the method of Zhang et al. is different from the MA method; therefore, we cannot simply compare their sample size with our result.

In Sect. 6.2.2, we apply the astrometric parallax measurement errors to the tracer stars. The distance errors deform the profiles of density fall-off and vertical velocity dispersion. Our result shows such faulty profiles can overestimate the LDMD. We estimate that the required precision of the parallax measurements is approximately $\sigma_\varpi \lesssim 0.1$ mas at $d = 1$ kpc in almost all cases. This required precision has not been achieved in present astrometric observations yet: Standard errors of *Hipparcos* observations are in the range of $\sigma_\varpi = 0.7$–0.9 mas even for stars brighter than 9th magnitude (mag) in a catalog published in 1997 (Perryman et al. 1997; Perryman 2012).[9] Since G11 have used the *Hipparcos* data for density profiles of their tracers, their tracer data are less precise than the required value. Although G11 did not use observed velocity data but introduced parametric runs for $\sigma^{\mathrm{obs}}_{z,\mathrm{trac}}(z)$, as we showed in Sect. 6.2.2, the LDMD can be overestimated solely by deformation of the tracer density profile caused by the distance errors. Therefore, we infer that the LDMD determined by G11 could be overestimated due to the imprecise astrometric measurements. Since G12 and Zhang et al. (2012) used photometric distances provided by Kuijken & Gilmore (1989a) and *Sloan Digital Sky Survey (SDSS)/SEGUE*, respectively, we cannot perform fair comparison with them.

It should be noted that our results may depend on details of our settings. For example, we arbitrarily set the scale height of our tracer to $h_{\mathrm{trac}} = 200$ pc. Besides, $z_{\mathrm{min}} = 0.2$ kpc and $z_{\mathrm{max}} = 1.2$ kpc are also arbitrary. In G11, their samples cover up to the height of $z_{\mathrm{max}} = 0.75$ kpc. It is expected that such a short sample can avoid high z regions where the observational errors become large. Figure 14 shows determined LDMDs in the cases of setting $z_{\mathrm{max}} = 0.75$ kpc. Here, the parallax measurement errors are taken into account. Although the overestimation of the LDMD is slightly mitigated in the case of the narrow cone sampling region, significantly high LDMDs are predicted when $A \geq 0.5$. Therefore, we still expect that the use of the *Hipparcos* sample causes overestimation even if tracer stars in the high z

---

[9] Although van Leeuwen & Fantino (2005) significantly improved the accuracy of the *Hipparcos* data, $\sigma_\varpi \lesssim 0.3$ mas can only be achieved for stars brighter than 6 mag (see also van Leeuwen 2005, 2007a,b).

regions are excluded. Our results conclude that the required parallax precisions are $\sigma_\varpi = 0.1$–0.3 mas.

In Sect. 6.2.3, we estimate the required precisions of proper motion measurements, which seem larger than 3 mas yr^{-1} at $d = 1$ kpc. In the cases of the cylindrical sampling regions, however, the required precision becomes severe: approximately $\sigma_\mu \leq 1$ mas yr^{-1} at $d = 1$ kpc for the narrow cylinder and $\sigma_\mu \leq 0.3$ mas yr^{-1} for the wide cylinder, respectively. Zhang et al. (2012) sampled their tracers in a wide cylinder the radius of which is 1 kpc. Their proper motion data taken from the *SDSS* catalog are as precise as $\simeq 3$ mas yr^{-1} for stars brighter than 18 mag in *r*-band (e.g., Bond et al. 2010). Their proper motion precisions would be insufficient for the wide cylinder sampling region *if* the MA method is used. However, since Zhang et al. (2012) determined the LDMD with their own method, we cannot conclude that their result is overestimating.

In Sect. 6.2.4, we estimate the required precisions of LOSV measurements and find that the LOSV errors lead to either overestimation or underestimation of the LDMD, which is contingent on distance-dependence of the errors. When we apply uniform errors: $\beta = 0$, the required precision is found to be ≤ 3.0 km s^{-1} for the cylindrical sampling regions and 5.0–7.5 km s^{-1} for the cylinder sampling regions. The required precision in this case corresponds to required precision floors in observations. Where the errors only weakly depend on distances, the LOSV errors can cause overestimation of the LDMD; whereas, in the cases of strong distance-dependence of the errors, the LOSV errors can cause underestimation. G12 used the sample of Kuijken & Gilmore (1989a), the LOSV errors of which are limited to < 10 km s^{-1} at $d = 1$ kpc. Therefore, their LOSV data would not cause underestimation or overestimation of the LDMD as long as $\beta \geq 2$ and their precision floors are sufficiently low.

To summarize our results, the parallax and proper motion uncertainties we examined can cause overestimation of the LDMD in calculation using the MA method. G11 have used the *Hipparcos* data, the parallax measurements of which are not precise enough to determine the LDMD accurately. On the other hand, G12 used the photometric distances. Therefore, we cannot fairly evaluate the reliability of their result. However, since G12 also resulted in the high LDMD which is consistent with G11, it is expected that G12 would also be overestimating. The LOSV data of G11 and G12 seem to be sufficiently precise. It is now interesting to return to Figure 1. In the right panel, the PDF of $\rho_{\rm dm}$–$\Sigma_{\rm s}$ inclines from the upper left to the lower right; the same trend can be seen in Figure 8 of G12. This means that $\rho_{\rm dm}$ and $\Sigma_{\rm s}$ have a correlation: When $\rho_{\rm dm}$ is overestimated, $\Sigma_{\rm s}$ would be underestimated. Figure 15 shows the PDFs in some cases where LDMDs are ill-determined. As we expected, $\Sigma_{\rm s}$ is underestimated when $\rho_{\rm dm}$ is overestimated and vice versa. In the results of G12, a baryonic surface density they determined is $\Sigma_{\rm s} = 45.5^{+5.6}_{-5.9}$ M$_\odot$ pc^{-2}, and an observed surface density they applied in their calculation is $\Sigma_{\rm s}^{\rm obs} = 49.4 \pm 4.6$ M$_\odot$ pc^{-2} (Flynn et al. 2006). Although the median value of the calculation is in the range of observational uncertainty, there could be small underestimation of $\Sigma_{\rm s}$. This may be a hint concerning the overestimation of the LDMD in G12. However, we emphasise our result that the MA method itself does not indicate any systematic biases and is capable of determining the LDMD with accuracy if sample size and observational precisions are sufficient (Sect. 6.1).

Our results, however, do not necessarily mean that the relatively low LDMDs suggested by the other previous studies are approved. Quality of the data used in G11 and G12 are not considerably inferior to the others. Although G11 and G12 demonstrated that methods of Holmberg & Flynn (2000) and Kuijken & Gilmore (1989a,b,c) have systematic biases to underestimate the LDMD, the other methods (e.g., the Zhang et al. (2012) method) and accuracies of their data should also be assessed carefully. For example, photometric distances may have systematic errors; Bovy et al. (2012d) have shown that stellar distances of G dwarfs determined with an isochrone of An et al. (2009) are nearly 10 % larger than those determined with an isochrone of Ivezić et al. (2008). Systematically large distances of tracer stars result in large scale heights of the distributions. Such thick tracers can underestimate the LDMD.

7.2. Validity of our galaxy modeling

We have to mention, however, that our analytical model to generate the mock data would be somewhat simplistic. For example, we assumed the galaxy model consisting of the 15 visible matter components. Such modeling may not necessarily well represent the real Galaxy. Bovy et al. (2012b,c,d) have recently discussed that the Galactic disk is composed of a lot of continuous "mono-abundance sub-populations" and that there are no distinct thin/thick disks. If this is the case, the stellar classification by Flynn et al. (2006, Table 3 in this paper) may not be suitable. In addition, as an observational difficulty, even if data are accurate and precise enough, it may be laborious to pick out kinematically homogeneous tracer stars and to verify the homogeneity. Contaminated tracer samples can lead to ill-determined LDMDs (e.g., Kuijken & Gilmore 1989a,b). This also needs reliable stellar population synthesis theory and spectroscopic observations.

The tracer in our study was modelled to have the uniform density and velocity distributions in a *z*-plane. Actually, stellar density and velocity dispersions in the Galaxy vary in the radial direction with scale radii of ~ 3.0 kpc (e.g., Lewis & Freeman 1989; Bovy et al. 2012d).[10] Therefore, if tracer-sampling regions are too wide, the kinematic homogeneity for the tracer can be broken in actual observations (see G11).

If our modeling can represent the real Galaxy well, our mock observations may be used to calibrate erroneously determined LDMDs. An advantageous point of astrometric observations is that observational uncertainties are already known. Therefore, even if sufficiently precise data are not available, our method can estimate magnitudes of under/overestimation of the ill-determined LDMDs by applying the known astrometric errors to the mock data.

7.3. Toward the future astrometric observations

Our results have shown that the MA method requires a high degree of astrometric precision to accurately determine the LDMD, which still cannot be achieved by present astrometric observations. The near-future astrometric satellite *Gaia*, however, will significantly exceed *Hipparcos*. *Gaia* is expected to observe the complete sample of all stars brighter than 20 mag with end-of-mission parallax precisions of $\simeq 0.01$ mas at $V = 10$ mag (V denotes Johnson V magnitude), 0.01–0.03 mas at $V = 15$ mag and up to 0.1–0.35 mas at $V = 20$ mag (e.g., de Bruijne et al. 2005; Bailer-Jones 2009; Jordi et al. 2010; Prusti 2012); proper motion precisions in the unit of mas yr^{-1} are comparable to the parallax precisions. A frequent tracer population is K dwarfs, the absolute magnitude of which are $V \sim 7$ mag (Binney & Merrifield

---

[10] Bovy et al. (2012c) have observationally shown that the scale radii of vertical velocity dispersions are as long as ~ 7.1 kpc.

1998). This means that K stars at $d = 1$ kpc have the brightness of $V \sim 17$ mag. Therefore, these stars are expected to be observed with the precisions of < 0.1 mas. Thus *Gaia* will be able to achieve the required astrometric precisions we estimated. Furthermore, *Gaia* is designed to measure LOSVs of the stars simultaneously. The LOSV precisions are 10–17 km s^{-1} at $V = 17$ mag with precision floors of $\simeq 1$ km s^{-1} (de Bruijne et al. 2005; Katz et al. 2004; Jordi et al. 2010), distance-dependence of which seems to be $\beta = 2$–3 (from comparison with Figure 7 of Prusti 2012). From comparing with Figure 11, *Gaia* seems to be able to determine the LDMD within the ranges of 90 % confidence levels although there may be slight underestimation if $\beta = 3$ and $C = 15$. Accordingly, *Gaia* is expected to enable determination of the LDMD using the MA method although it may be better to replace the LOSV data with more precise measurements.

In addition to *Gaia*, *Nano-JASMINE* and *JMAPS* are also individually planned to produce all-sky astrometric catalogs. By combining their data with the *Hipparcos* and *Tycho* positional data from 1991, proper motions with 0.1 mas yr^{-1} are expected to be achievable for bright stars (Michalik et al. 2012). Such a high precision astrometry would improve not only the LDMD determination but also our understanding of various aspects of Galactic dynamics.

8. Conclusions

We scrutinized the MA method devised by Garbari et al. and carefully assessed their LDMD determinations. We created mock observational data and applied the MA method. As results, we found that the MA method is capable of determining the LDMD with accuracy if the sample size of a tracer and observational precisions are sufficient. We found that the sample size must be larger than approximately 6,000 stars. Astrometric errors, however, can cause overestimation on the LDMD determination, and we estimated that the required precisions are approximately 0.1–0.3 mas for parallax measurements. Proper motion precisions do not seem to be as important as the parallax precisions. In addition, LOSV errors can cause either overestimation or underestimation of the LDMD determination: If the errors weakly or strongly depend on distance, the LDMD can be overestimated or underestimated, respectively. Although the required precisions of LOSV measurements are also contingent on the distance-dependence of the errors (see Sect. 6.2.4 and Figure 10 and 11 for details).

From our results, we infer that G11 who used *Hipparcos* data would be overestimating the LDMD due to the insufficient astrometric precisions. Moreover, although the LDMD determined by G12 who used photometric distances is consistent with the result of G11, the sample size of G12 would not be large enough to precisely determine the LDMD. However, our results do not necessarily mean that other previous studies displaying a preference for relatively low LDMDs (e.g., Zhang et al. 2012; Bovy & Tremaine 2012) are satisfactory. Careful scrutinizations for the other methods to determine the LDMD are also needed.

The near-future astrometric satellite *Gaia* can be expected to measure parallaxes, proper motions and LOSVs with sufficient precisions. Our results indicate that *Gaia* will provide data that enables us to determine the LDMD using the MA method.

Acknowledgements. The authors appreciate Taihei Yano, Shingo Kahima and Takuji Hara for their helpful discussion. Numerical computations and data analyses were in part carried on analysis server system at Center for Computational Astrophysics, CfCA, of National Astronomical Observatory of Japan. This research was partially supported by the Ministry of Education, Science, Sports and Culture, Grant-in-Aid for Scientific Research (A), No.23244034, 2011-2015.

References

Allen, C. & Martos, M. A. 1986, Rev. Mexicana Astron. Astrofis., 13, 137
Allen, C. & Santillan, A. 1991, Rev. Mexicana Astron. Astrofis., 22, 255
Allgood, B., Flores, R. A., Primack, J. R., et al. 2006, MNRAS, 367, 1781
An, D., Pinsonneault, M. H., Masseron, T., et al. 2009, ApJ, 700, 523
Bahcall, J. N. 1984a, ApJ, 287, 926
Bahcall, J. N. 1984b, ApJ, 276, 169
Bahcall, J. N. 1984c, ApJ, 276, 156
Bailer-Jones, C. A. L. 2009, in IAU Symposium, Vol. 254, IAU Symposium, ed. J. Andersen, Nordströara, B. m, & J. Bland-Hawthorn, 475–482
Baudis, L. 2012, Physics of the Dark Universe, 1, 94
Bett, P., Eke, V., Frenk, C. S., et al. 2007, MNRAS, 376, 215
Bienayme, O., Robin, A. C., & Creze, M. 1987, A&A, 180, 94
Binney, J. & Merrifield, M. 1998, Galactic Astronomy (Princeton: Princeton Univ. Press)
Binney, J. & Tremaine, S. 2008, Galactic Dynamics Second Edition (Princeton: Princeton Univ. Press)
Bond, N. A., Ivezić, Ž., Sesar, B., et al. 2010, ApJ, 716, 1
Bovy, J., Allende Prieto, C., Beers, T. C., et al. 2012a, ApJ, 759, 131
Bovy, J., Rix, H.-W., & Hogg, D. W. 2012b, ApJ, 751, 131
Bovy, J., Rix, H.-W., Hogg, D. W., et al. 2012c, ApJ, 755, 115
Bovy, J., Rix, H.-W., Liu, C., et al. 2012d, ApJ, 753, 148
Bovy, J. & Tremaine, S. 2012, ApJ, 756, 89
Branham, Jr., R. L. 2010, MNRAS, 409, 1269
Catena, R. & Ullio, P. 2010, J. Cosmology Astropart. Phys., 8, 4
Creze, M., Chereul, E., Bienayme, O., & Pichon, C. 1998, A&A, 329, 920
Creze, M., Robin, A. C., & Bienayme, O. 1989, A&A, 211, 1
de Bruijne, J., Perryman, M. A. C., Lindegren, L., et al. 2005, Technical Note Gaia-JdB-022, http://www.rssd.esa.int/index.php?project=Gaia
Debattista, V. P., Roskar, R., Valluri, M., et al. 2013, preprint (astro-ph/1301.2670)
Deg, N. & Widrow, L. 2013, MNRAS, 428, 912
Dubinski, J. & Carlberg, R. G. 1991, ApJ, 378, 496
Fellhauer, M., Belokurov, V., Evans, N. W., et al. 2006, ApJ, 651, 167
Flynn, C. & Fuchs, B. 1994, MNRAS, 270, 471
Flynn, C., Holmberg, J., Portinari, L., Fuchs, B., & Jahreiß, H. 2006, MNRAS, 372, 1149
Garbari, S., Liu, C., Read, J. I., & Lake, G. 2012, MNRAS, 425, 1445
Garbari, S., Read, J. I., & Lake, G. 2011, MNRAS, 416, 2318
Gaume, Jr., R. A., Dorland, B., Hennessy, G., et al. 2009, in Bulletin of the American Astronomical Society, Vol. 41, American Astronomical Society Meeting Abstracts #213, #451.01
Gilmore, G. & Reid, N. 1983, MNRAS, 202, 1025
Gouda, N. 2011, Scholarpedia, 6(10), 12021, http://www.scholarpedia.org/article/JASMINE
Gregory, P. 2010, Bayesian Logical Data Analysis for the Physical Sciences
Helmi, A. 2004, ApJ, 610, L97
Hill, E. R. 1960, Bull. Astron. Inst. Netherlands, 15, 1
Holmberg, J. & Flynn, C. 2000, MNRAS, 313, 209
Holmberg, J. & Flynn, C. 2004, MNRAS, 352, 440
Ibata, R., Lewis, G. F., Irwin, M., Totten, E., & Quinn, T. 2001, ApJ, 551, 294
Ibata, R., Lewis, G. F., Martin, N. F., Bellazzini, M., & Correnti, M. 2012, preprint (astro-ph/1212.4958)
Irrgang, A., Wilcox, B., Tucker, E., & Schiefelbein, L. 2013, A&A, 549, A137
Ivezić, Ž., Sesar, B., Jurić, M., et al. 2008, ApJ, 684, 287
Jordi, C. et al. 2010, A&A, 523, A48
Katz, D. et al. 2004, MNRAS, 354, 1223
Kotoneva, E., Flynn, C., Chiappini, C., & Matteucci, F. 2002, MNRAS, 336, 879
Kuhlen, M., Diemand, J., & Madau, P. 2007, ApJ, 671, 1135
Kuijken, K. 1991, ApJ, 372, 125
Kuijken, K. & Gilmore, G. 1989a, MNRAS, 239, 605
Kuijken, K. & Gilmore, G. 1989b, MNRAS, 239, 651
Kuijken, K. & Gilmore, G. 1989c, MNRAS, 239, 571
Law, D. R. & Majewski, S. R. 2010, ApJ, 714, 229
Lewis, J. R. & Freeman, K. C. 1989, AJ, 97, 139
Lutz, T. E. & Kelker, D. H. 1973, PASP, 85, 573
Michalik, D., Lindegren, L., Hobbs, D., Lammers, U., & Yamada, Y. 2012, in Astronomical Society of the Pacific Conference Series, Vol. 461, Astronomical Data Analysis Software and Systems XXI, ed. P. Ballester, D. Egret, & N. P. F. Lorente, 549
Mignard, F. 2000, A&A, 354, 522
Moni Bidin, C., Carraro, G., Méndez, R. A., & Smith, R. 2012, ApJ, 751, 30
Olling, R. P. & Merrifield, M. R. 2000, MNRAS, 311, 361

Olling, R. P. & Merrifield, M. R. 2001, MNRAS, 326, 164
Oort, J. H. 1932, Bull. Astron. Inst. Netherlands, 6, 249
Oort, J. H. 1960, Bull. Astron. Inst. Netherlands, 15, 45
Perryman, M. 2012, Astronomical Applications of Astrometry
Perryman, M. A. C., de Boer, K. S., Gilmore, G., et al. 2001, A&A, 369, 339
Perryman, M. A. C. et al. 1997, A&A, 323, L49
Pham, H.-A. 1997, in ESA Special Publication, Vol. 402, Hipparcos - Venice '97, ed. R. M. Bonnet, E. Høg, P. L. Bernacca, L. Emiliani, A. Blaauw, C. Turon, J. Kovalevsky, L. Lindegren, H. Hassan, M. Bouffard, B. Strim, D. Heger, M. A. C. Perryman, & L. Woltjer, 559–562
Prusti, T. 2012, Astronomische Nachrichten, 333, 453
Read, J. I., Mayer, L., Brooks, A. M., Governato, F., & Lake, G. 2009, MNRAS, 397, 44
Salucci, P., Nesti, F., Gentile, G., & Frigerio Martins, C. 2010, A&A, 523, A83
Smith, H. 2003, MNRAS, 338, 891
Sofue, Y. 2012, PASJ, 64, 75
Sofue, Y., Honma, M., & Omodaka, T. 2009, PASJ, 61, 227
Spooner, N. J. C. 2007, Journal of the Physical Society of Japan, 76, 111016
van Leeuwen, F. 2005, A&A, 439, 805
van Leeuwen, F., ed. 2007a, Astrophysics and Space Science Library, Vol. 350, Hipparcos, the New Reduction of the Raw Data
van Leeuwen, F. 2007b, A&A, 474, 653
van Leeuwen, F. & Fantino, E. 2005, A&A, 439, 791
Weber, M. & de Boer, W. 2010, A&A, 509, A25
Zemp, M., Diemand, J., Kuhlen, M., et al. 2009, MNRAS, 394, 641
Zhang, L., Rix, H.-W., van de Ven, G., et al. 2012, preprint (astro-ph/1209.0256)

Appendix A: Validity of the isothermality for the deduced model

Deduced galaxy models of G11 and G12 are slightly different from each other. G11 has used parametrized runs of velocity dispersions assuming a behavior similar to the observational fitting by Bond et al. (2010). G12, on the other hand, assumed that all components are isothermal. Here, we discuss the impact of these velocity dispersion profiles on the calculation of the MA method. In addition, we verify the appropriateness of the isothermal assumption used in G12 and this study.

The dispersion runs introduced in G11 is described by a quadratic form:

$$\sigma_{z,i}^2(z) = \sigma_{z,i}^2(0)\left(1 + cz^2\right), \tag{A.1}$$

where the constant of c is chosen so that this function satisfies the observational fitting of Bond et al. (2010):

$$\sigma_{z,i}(z_{\max}) = \sigma_{z,i}(0) + 4\left(\frac{z_{\max}}{\mathrm{kpc}}\right)^{1.5}. \tag{A.2}$$

Figure A.1 shows comparison between the quadratic functions and the analytical solutions of the Jeans equation for some model components. Although some components seem to be fitted well by the quadratic functions, some others are fitted poorly. This would be due to the fact that the observations of Bond et al. (2010) are for blue disk stars and/or our assumed model is artificial.

We set all parameters of $\rho_i(0)$, $\sigma_{z,i}(0)$ and $\rho_{\rm dm}$ to the true values and compute surface density profiles of the deduced models, $(4\pi G)^{-1}\mathrm{d}\Phi/\mathrm{d}z$, following the procedure of Sect. 2.1 with the quadratic functions and the isothermality. Figure A.2 shows the results. In the top panel, we compare the results with the assumed density profile of Eq. (11). Since all of them are almost consistent, it can be said that both the quadratic functions and the isothermality can reproduce well the assumed galactic potential. The bottom panel shows fractional differences between the results and the assumed model. In both cases, the deduced models underestimate the surface density in $z \lesssim 0.2$ kpc and overestimate in $z \gtrsim 0.2$ kpc. However, magnitudes of the overestimation at $z_{\max}$ are only ~ 0.5 % and ~ 1.5 % in the cases of the isothermal and the quadratic dispersions, respectively. From these results, we can see that the isothermality for the deduced model hardly affects the determination of the LDMD. In addition, the runs of velocity dispersions of the model components do not seem to be important. G11 have also come to the same conclusion and they mentioned as follows: Although the velocity dispersion profile of the tracer directly affects the tracer density fall-off and has significant impact on the result, uncertainties in dispersion profiles of the model components are, by contrast, marginalized out when we calculate $\rho_{\rm dm}$ and $\rho_{\rm s}(0)$, since they appear only in Eq. (8) through Eq. (3). From the above results, it is verified that assuming isothermality for the model components does not lead to erroneous determinations of the LDMD. Although the quadratic function used in G11 is not necessarily better than the isothermal approximation, the impact of the difference between them seems trivial.

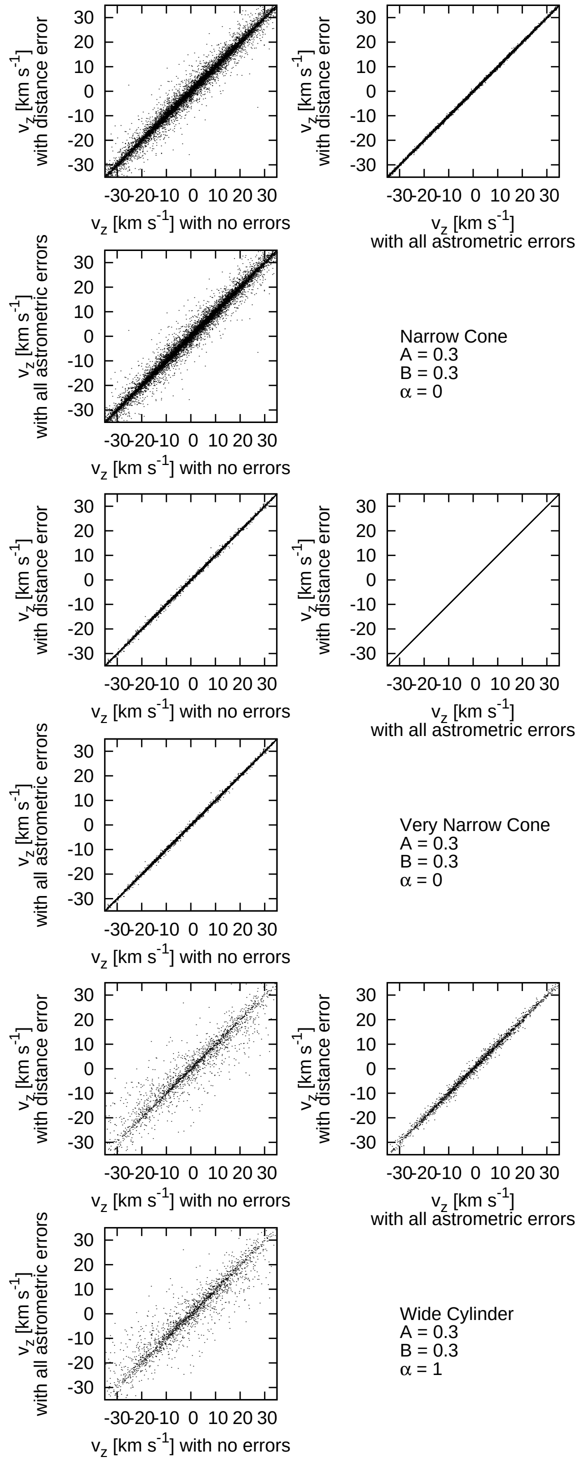

Fig. 8. Influence of distance and proper motion errors on vertical velocities of the tracer stars in three example cases. In each three panels, the top left panel compares true v_z and those affected by the distance errors alone. The top right panel compares the v_z affected by the distance errors and those affected by both the distance and the proper motion errors. The bottom left panel shows the true v_z and those affected by both errors.

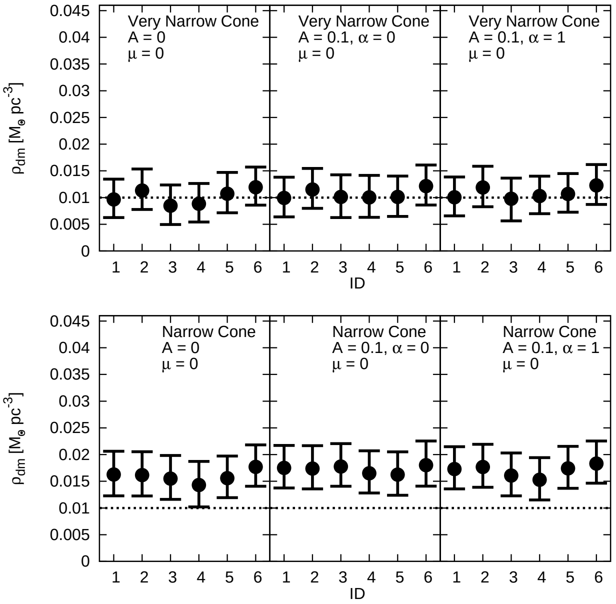

Fig. 9. LDMDs determined in the cases of ignoring the proper motion measurement. Here we set $\mu_\theta = 0$ for all tracer stars.

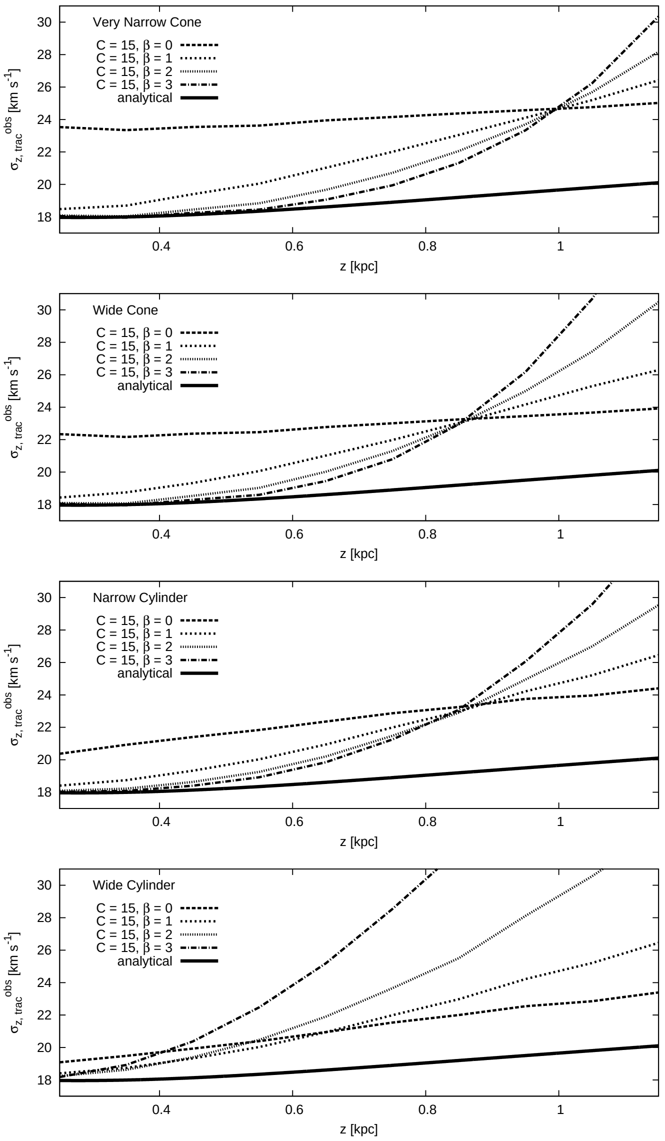

Fig. 12. Changes of vertical velocity dispersion profiles of the tracer by the LOSV errors. Here we used mock data of one million stars.

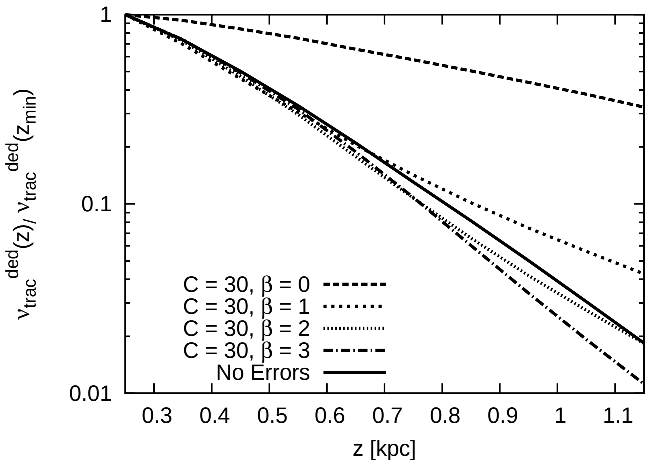

Fig. 13. Tracer density fall-offs deduced by the MA method. Here we set all parameters to the true values and apply the LOSV errors only. Because distance errors are not taken into account, the deduced profile in the case of no errors corresponds to the observed density fall-off. The mock data of one million stars are used.

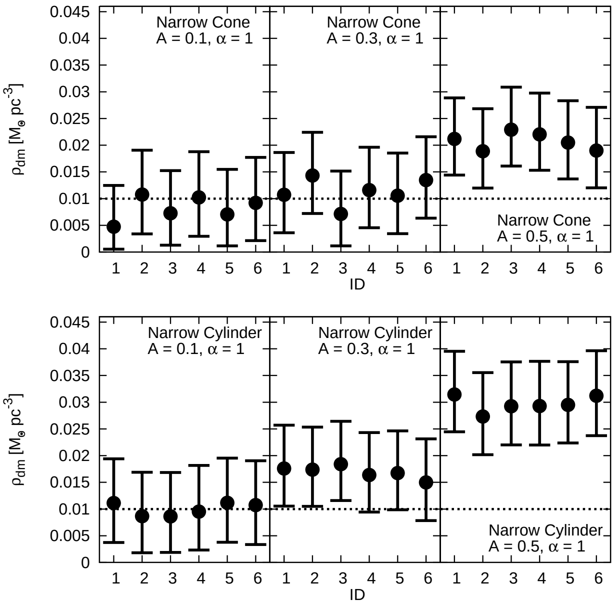

Fig. 14. Influence of the distance errors on determining the LDMD in the cases of $z_{max} = 0.75$ kpc. The other settings are the same.

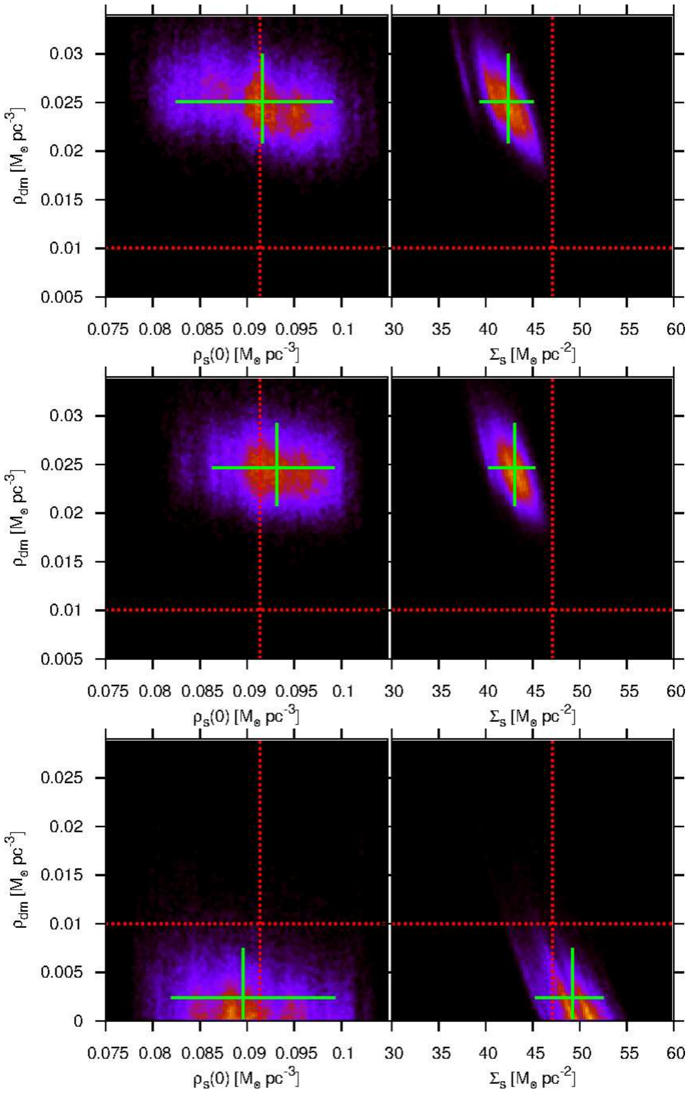

Fig. 15. PDFs of LDMD, local and surface densities of the visible matters. The red and green lines are the same as in Figure 1. The top panel shows the result in the case of the narrow cone sampling region with $A = 0.3$, $B = C = 0$, $\alpha = 0$ and the sample ID = 1. This case overestimates the LDMD. The middle panel shows the result in the case of the wide cylinder sampling region with $A = 0.1$, $B = 2.0$ $C = 0$, $\alpha = 0$ and the sample ID = 1. This case overestimates the LDMD. The bottom panel from the top shows the result in the case of the narrow cylinder sampling region with $A = B = 0$, $C = 30.0$, $\beta = 3$ and the sample ID = 1. This case underestimates the LDMD.

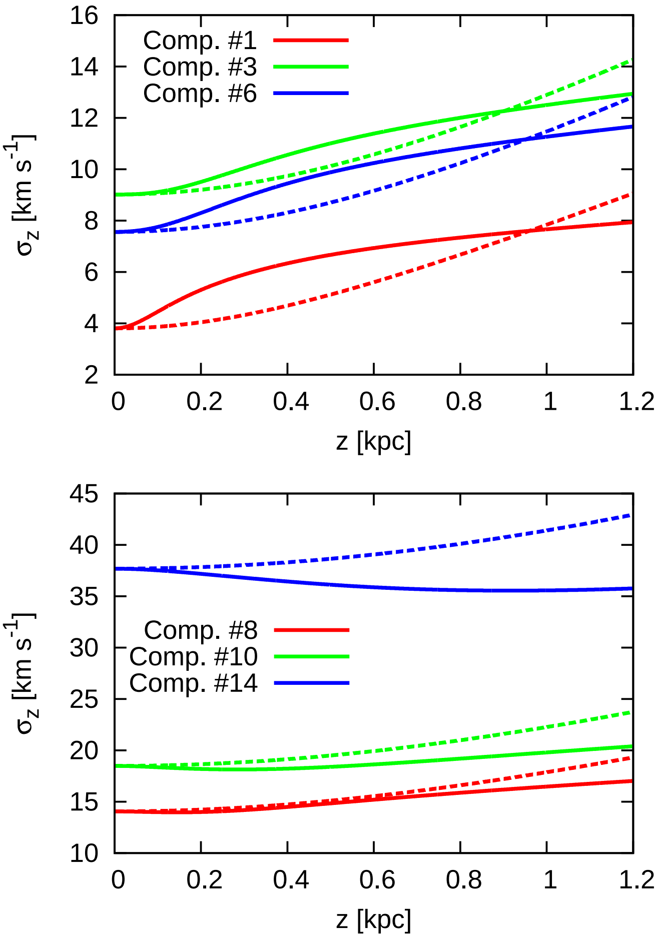

Fig. A.1. Velocity dispersion profiles of some model components in Table 1. The solid and dashed lines indicate analytical solutions computed by Eq. (12) and fittings by the quadratic function, respectively.

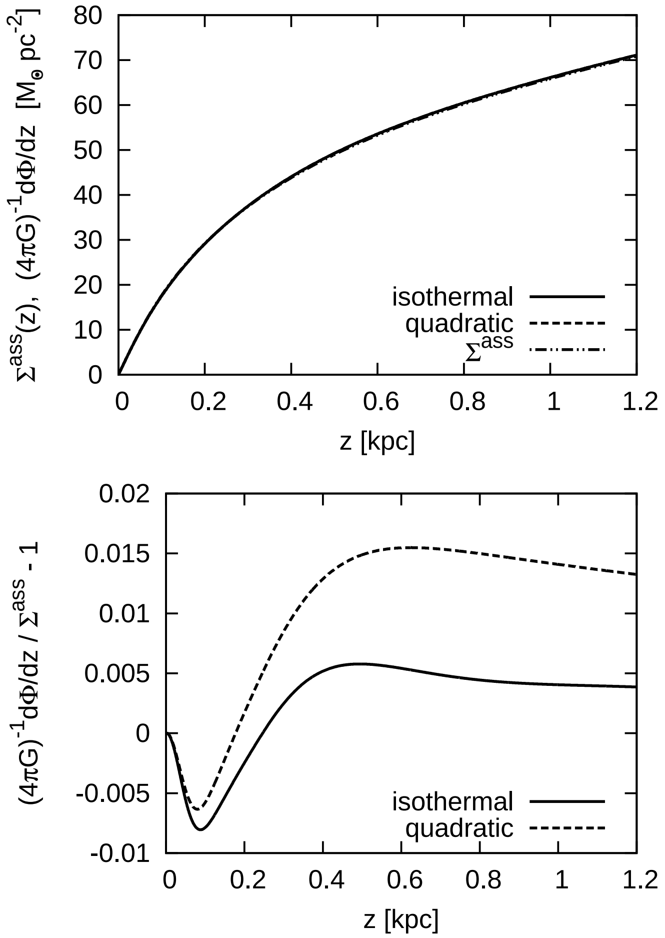

Fig. A.2. Comparison between surface densities deduced from the Jeans and Poisson equations, $(4\pi G)^{-1}\mathrm{d}\Phi/\mathrm{d}z$, and the density profile assumed in the model, Σ^{ass}. The top panel indicates the surface density profiles. Since the three lines almost overlap, they may be indistinguishable by eye. The bottom panel shows fractional differences between the deduced surface density profiles and the assumed model.

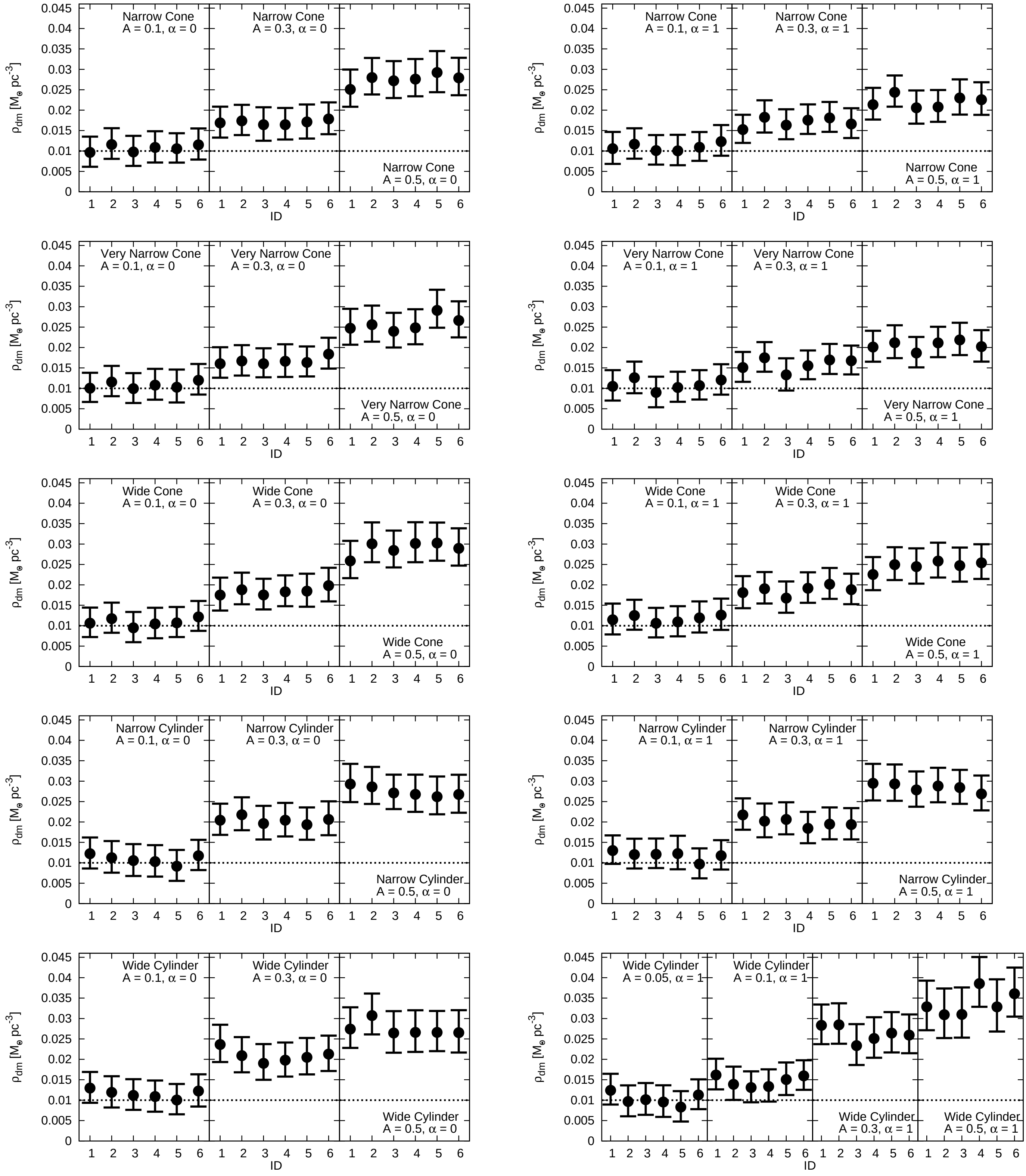

Fig. 5. Influence of the astrometric distance errors on determining the LDMD. The left and right panels indicate the results of adopting $\alpha = 0$ and $\alpha = 1$, respectively. In each case, we conduct the same computation with different tracer samples generated in the same conditions (ID = 1–6). The horizontal dotted line indicates the true LDMD. In the case of the wide cylinder with $\alpha = 1$ (the right bottom panel), we additionally show the result of adopting $A = 0.05$.

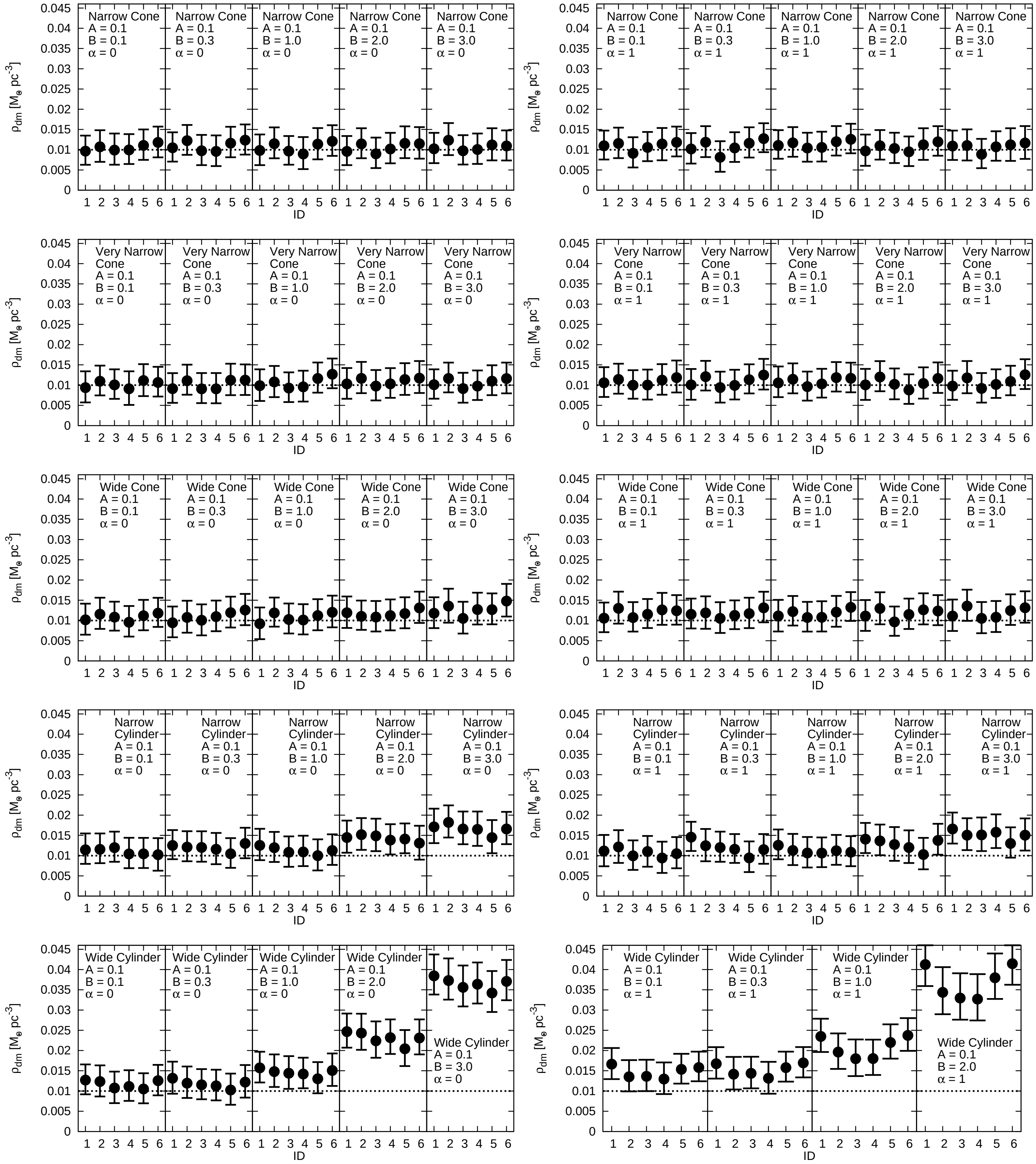

Fig. 7. Influence of the proper motion errors on determining the LDMD. The left and right panels indicate the results of adopting $\alpha = 0$ and $\alpha = 1$, respectively. In all cases, we set the magnitude of distance error to be $A = 0.1$. In each case, we conduct the same computations with different tracer samples generated from the same conditions (ID = 1 – 6). The horizontal dotted line indicates the true LDMD. In the case of the wide cylinder with $\alpha = 1$ (the right bottom panel), we omit the result of adopting $B = 3.0$ since derived LDMDs become extremely high.

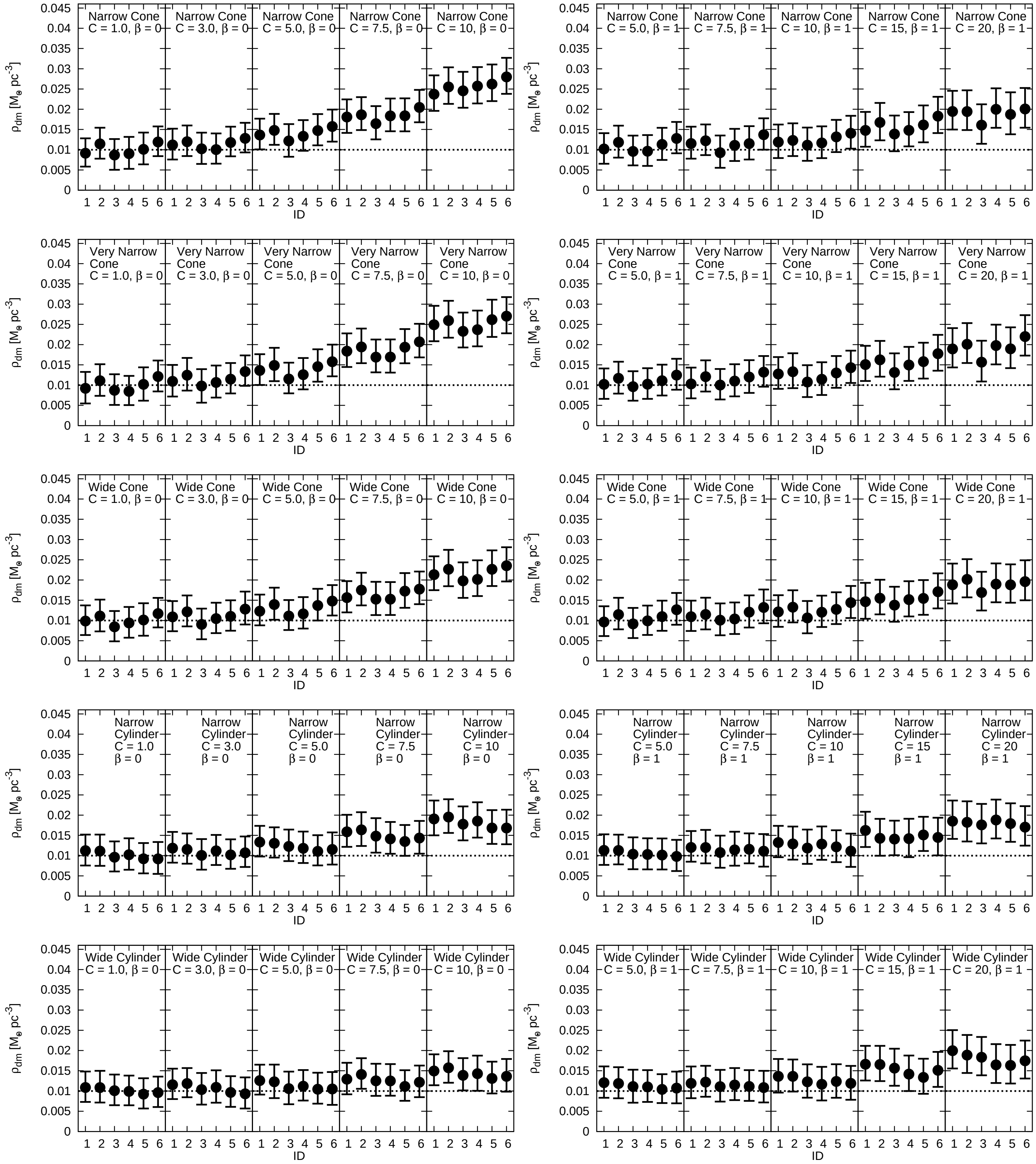

Fig. 10. Influence of the LOSV errors on determining LDMD. The left and right panels indicate the results of adopting $\beta = 0$ and $\beta = 1$, respectively. In all cases, we assume that there are no distance and proper motion errors: $A = B = 0$. In each case, we conduct the same computations with different tracer samples generated from the same conditions (ID = 1 – 6). The horizontal dotted line indicates the true LDMD.

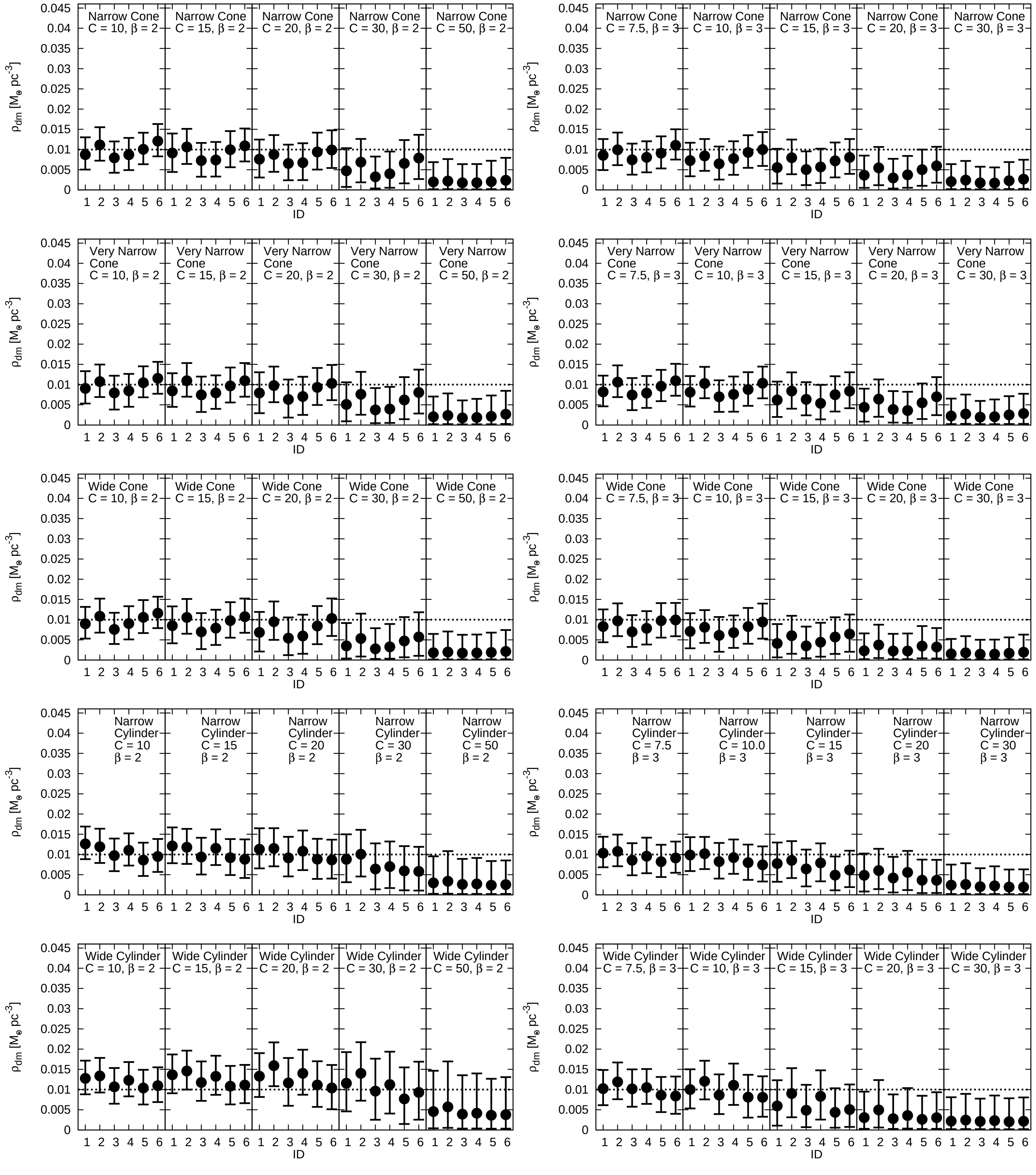

Fig. 11. Same as Figure 10 but adopting $\beta = 2$ (left panels) and $\beta = 3$ (right panels).